Journal of Molecular Structure 1282 (2023) 135258

Contents lists available at ScienceDirect

Journal of Molecular Structure

journal homepage: www.elsevier.com/locate/molstr

$[Cu_2(ox)(dien)_2](NO_3)_3$, a precursor for preparation of CuO nanoparticles: Synthesis, structural, Hirshfeld surface analyses, and physico-chemical investigations

Mohamed Akouibaa[a], Imane Lakkab[a], Amani Direm[b,c], Mohammed Lachkar[a], Rachid Ouarsal[a], Souâd Rakib[a], Vesim Nasif[d], Koray Sayin[d], Nicola Morley[e], Brahim El Bali[f,*]

[a] Engineering Laboratory of Organometallic, Molecular Materials, and Environment, Faculty of Sciences, University Sidi Mohamed Ben Abdellah, 30000 Fez, Morocco
[b] Laboratory of Structures, Properties and Interatomic Interactions LASPI²A, Faculty of Sciences and Technology, Abbes Laghrour University, Khenchela 40000, Algeria
[c] Department of Matter Sciences, Faculty of Sciences and Technology, Abbes Laghrour University, Khenchela 40000, Algeria
[d] Department of Chemistry, Faculty of Science, Sivas Cumhuriyet University 58140 Sivas – Turkey, Turkey
[e] Department of Materials Science and Engineering, University of Sheffield, Sheffield S1 3JD, United Kingdom
[f] Independent Scientist, Marrakech, Morocco

ARTICLE INFO

Article history:
Received 13 December 2022
Revised 25 February 2023
Accepted 27 February 2023
Available online 28 February 2023

Keywords:
Oxalato-bridged complexes
Crystal structure
Nanoparticles
Magnetic properties
Antioxidant activity
Hirshfeld surface and topological analyses

ABSTRACT

$[Cu_2(ox)(dien)_2](NO_3)_3$ with (ox=oxalate, dien=diethylenetriamine) has been synthesized and characterized by single-crystal X-ray diffraction as well as FTIR and UV–Vis spectroscopic techniques. The complex crystallizes in the monoclinic space group (P2/c) with the following cell parameters (Å, °): a = 23.7888(10), b = 6.7055(3), c = 12.7842(6) and β = 95.534(2). The 3D network consists of (C_2O_4) groups bridging binuclear Cu(II) cations, in which the copper atoms are in a distorted square-pyramidal coordination environment. Experimental and computed FT-IR results confirmed the presence of characteristic bands of diethylenetriamine tridentate, nitrate and oxalate bidentate groups. UV–Vis spectrum of the complex was recorded and the characteristic transitions were determined. TG-DSC measurements revealed thermal stability of the studied complex until 473 K. Calcination of the complex under air led to the production of CuO nanoparticles. Moreover, the morphology and the size of the complex and its CuO nanoparticles were monitored by scanning electron microscopy (SEM). Magnetization and a.c. susceptibility were measured and discussed. The complex molecular structure was optimized and the simulated geometric parameters compared with the crystal structure values. *Hirshfeld* surface and topological analyses were performed to describe the intermolecular interactions and to simplify the 3D networks of $[Cu_2(ox)(dien)_2](NO_3)_3$. Moreover, its antioxidant activity was assessed using DPPH, ferric reducing power tests and phosphomolybdenum assay.

1. Introduction

The chemistry of oxalate-containing compounds has shown a large interest and has become an active area of research in the past decades, thanks to its relevant coordination properties and its ability to bind many metal ions in bis-chelating bridging mode. The oxalate anion $(C_2O_4)^{2-}$ has a wide application area such as catalysis [1,2] and biological chemistry [3]. In this last field, the oxalate ion $(C_2O_4)^{2-}$ has been investigated to analyze its capability to mediate the exchange coupling between first-row transition metal ions separated by more than 5 Å in both homo- [4–7] and heteropolynuclear [8–10] compounds. A great number of oxalato-bridged binuclear complexes have been characterized so far [11–16]. Such as oxalato-bridged homometallic copper (II) compounds [17–36], where (C_2O_4) is binding the two metallic centers in bis-bidentate bridging mode [17,19-34]. Analysis of the factors that influence the extent of the coupling through oxalate allowed to tune the value of the singlet-triplet energy gap (J) in oxalato-bridged binuclear copper (II) in which the separation distance between the metal ions is in the range 5–6 Å, as reported in the literature [23,31-33] ($|J|$= 12–76 cm^{-1}). However, large J values ($|J|$ = 274–424 cm^{-1}) were reported in the following papers

* Corresponding author.
E-mail address: b_elbali@yahoo.com (B.E. Bali).

https://doi.org/10.1016/j.molstruc.2023.135258
0022-2860/

Table 1
Crystal data and structure refinement parameters for $[Cu_2(ox)(dien)_2](NO_3)_3$.

Parameters	Complex $[Cu_2(ox)(dien)_2](NO_3)_3$
Chemical formula	$C_{10}H_{26}Cu_2N_6O_4{\cdot}3(NO_3)$
M_r (g.mol^{-1})	607.45
Crystal system, space group	Monoclinic, *P2/c*
Temperature (K)	150
a (Å), b (Å), c (Å)	23.7888 (10), 6.7055 (3), 12.7842 (6)
α (°), β (°), γ (°)	90, 95.534 (2), 90
V (Å^3), Z	2029.78 (16), 4
Radiation type	Mo $K\alpha$
μ (mm^{-1})	2.16
Crystal size (mm)	0.17 × 0.13 × 0.04
θ Range (°)	2.6–28.2
D_x (g.cm^{-3})	1.785
F(000)	1120
Index range	$-31\leq h\leq 31$; $-8\leq k\leq 8$; $-17\leq l\leq 16$
Diffractometer	Bruker D8 VENTURE
Absorption correction	Multi-scan: SADABS2016/2 (Bruker, 2016/2) was used for absorption correction.
T_{min}; T_{max}	0.658; 0.738
No. of measured, independent and observed [$I > 2\sigma(I)$] reflections	22,561, 5000, 4080
R_{int}	0.073
Refinement method	Least-squares matrix: full
$R[F^2 > 2\sigma(F^2)]$, $wR_2(F^2)$, S	0.037, 0.099, 1.04
No. of reflections	5000
No. of parameters	273
$\Delta\rho_{max}$, $\Delta\rho_{min}$ (e.Å^{-3})	0.51, −0.50

Table 2
Fractional atomic coordinates and isotropic or equivalent isotropic displacement parameters (Å^2) for $[Cu_2(ox)(dien)_2](NO_3)_3$.

	x	*y*	*z*	U_{iso}*/U_{eq}
Cu1	0.82852 (2)	0.69168 (5)	0.86215 (2)	0.01706 (9)
Cu2	0.67187 (2)	0.23727 (5)	0.62983 (2)	0.01600 (9)
N1	0.82847 (9)	0.9142 (3)	0.75718 (17)	0.0240 (5)
H1A	0.812932	0.871148	0.693320	0.029*
H1B	0.807341	1.017603	0.777734	0.029*
N4	0.91022 (8)	0.7559 (3)	0.89313 (16)	0.0194 (4)
H4	0.932294	0.662430	0.851873	0.023*
N7	0.83741 (9)	0.5432 (3)	0.99867 (16)	0.0251 (5)
H7A	0.819039	0.608849	1.047540	0.030*
H7B	0.822144	0.419142	0.989944	0.030*
N8	0.66407 (8)	0.4211 (3)	0.50571 (15)	0.0207 (4)
H8A	0.680367	0.540662	0.523525	0.025*
H8B	0.681919	0.368074	0.452346	0.025*
N11	0.58896 (8)	0.1951 (3)	0.59852 (15)	0.0178 (4)
H11	0.569014	0.284023	0.645745	0.021*
N14	0.66993 (8)	−0.0063 (3)	0.72028 (16)	0.0212 (4)
H14A	0.688045	−0.108892	0.691232	0.025*
H14B	0.687652	0.018660	0.785257	0.025*
C2	0.88737 (11)	0.9818 (4)	0.7491 (2)	0.0260 (6)
H2A	0.887599	1.122666	0.726001	0.031*
H2B	0.905176	0.899503	0.697083	0.031*
C3	0.91947 (11)	0.9604 (4)	0.8561 (2)	0.0271 (6)
H3A	0.960245	0.984088	0.851607	0.033*
H3B	0.905678	1.058636	0.905489	0.033*
C5	0.92630 (12)	0.7191 (5)	1.0062 (2)	0.0301 (6)
H5A	0.913647	0.830972	1.048742	0.036*
H5B	0.967825	0.706659	1.019943	0.036*
C6	0.89799 (11)	0.5276 (5)	1.0346 (2)	0.0318 (6)
H6A	0.914898	0.412996	1.000180	0.038*
H6B	0.903133	0.506758	1.111604	0.038*
C9	0.60354 (10)	0.4499 (4)	0.4712 (2)	0.0256 (5)
H9A	0.598619	0.485923	0.395790	0.031*
H9B	0.587973	0.559019	0.511871	0.031*
C10	0.57291 (11)	0.2565 (4)	0.4892 (2)	0.0259 (6)
H10A	0.531553	0.276613	0.477367	0.031*
H10B	0.583869	0.152628	0.440026	0.031*
C12	0.57664 (11)	−0.0136 (4)	0.6248 (2)	0.0259 (6)
H12A	0.587951	−0.104293	0.569393	0.031*
H12B	0.535728	−0.030940	0.630529	0.031*
C13	0.60996 (11)	−0.0598 (4)	0.7286 (2)	0.0256 (6)
H13A	0.594952	0.017963	0.785603	0.031*
H13B	0.606837	−0.203371	0.745120	0.031*
O1A	0.82370 (7)	0.4396 (3)	0.74657 (13)	0.0202 (4)
O2A	0.74597 (7)	0.6484 (3)	0.84250 (13)	0.0198 (4)
O3A	0.75549 (7)	0.2715 (3)	0.65348 (13)	0.0182 (4)
O4A	0.67762 (7)	0.4725 (3)	0.75494 (13)	0.0209 (4)
C1A	0.77331 (9)	0.3985 (3)	0.72139 (17)	0.0151 (4)
C2A	0.72766 (9)	0.5165 (3)	0.77722 (17)	0.0159 (4)
O1N	0.78046 (11)	0.1243 (4)	0.9371 (2)	0.0595 (7)
O2N	0.74601 (8)	0.2318 (3)	1.07622 (14)	0.0279 (4)
O3N	0.69456 (8)	0.0526 (3)	0.96316 (15)	0.0385 (5)
N1N	0.74036 (9)	0.1337 (3)	0.99174 (16)	0.0250 (5)
O4N	1.000000	0.6600 (4)	0.750000	0.0446 (8)
O5N	0.96926 (9)	0.3856 (3)	0.80758 (17)	0.0425 (5)
N2N	1.000000	0.4754 (5)	0.750000	0.0238 (7)
O6N	0.52789 (8)	0.5487 (3)	0.68777 (16)	0.0394 (5)
O7N	0.500000	0.2741 (5)	0.750000	0.0621 (11)
N3N	0.500000	0.4589 (5)	0.750000	0.0233 (6)

[20,30,34]. By taking advantage of copper (II) coordination sphere's plasticity [37,38], the variation of the orientation and symmetry of the molecular orbitals describing the unpaired electron Cu^{2+} is considered as a crucial parameter for the enhancement of copper (II) complexes' stereochemistry. On the other side, the oxalato-bridged Ni(II) complexes adopt octahedral geometry whereas the corresponding |J| values vary in the range from 17 to 39 cm^{-1} [27-29,35,36]. In these complexes, the magnitude of the magnetic coupling J strongly depends on the nature of the blocking ligands' donor atoms coordinated to the central metal ion.

As a continuation of our previous researches on synthesis and investigation of coordination compounds [11,39-42], we report herein the chemical preparation, spectroscopic characterization in correlation with the crystal structure X-ray diffraction data and thermal stability of a new oxalato-bridged binuclear Cu(II) complex based on linear tridentate amine, namely diethylenetriamine, as blocking ligands. Furthermore, we aimed to investigate the formation of CuO nanoparticles from the studied complex, which were obtained under air atmosphere, as these may be suitable for particular usage in various fields of science [43,44]. Furthermore, we discuss herein the magnetization and a.c. susceptibility of the complex as well as its optimized molecular structure and frontier molecular orbitals. We explore the leading intermolecular interactions and simplify the structural packaging using *Hirshfeld* surface and topological analyses. For the best of our knowledge, we study for the first time the antioxidant activity of $[Cu_2(ox)(dien)_2](NO_3)_3$.

2. Experimental

2.1. Synthesis of complex $[Cu_2(ox)(dien)_2](NO_3)_3$

Single crystals of the complex $[Cu_2(ox)(dien)_2](NO_3)_3$ were synthesized under ambient conditions. The reaction mixture of copper(II) nitrate hexahydrate (0.25 g, 1.025 mmol), dissolved in distilled water (10 mL), was added dropwise to an aqueous solution (15 mL) of oxalic acid (0.15 g, 1.189 mmol) at room temperature with continuous stirring. Diethylenetriamine (2.5 mL, 24.23 mmol) diluted in distilled water (10 mL) was then added dropwise. The blue solution was allowed to evaporate slowly at room temperature until dark blue single crystals were formed. Being very soluble in water, the crystals were washed several times with ethanol and dried in open air.

2.2. Preparation of copper oxide CuO nanoparticles

Sufficient quantities of the complex were used as a precursor to synthesize CuO nanoparticles. For this purpose, the blue sediment of this complex was placed in porcelain crucible at temperature above 725 °C for 2 h, after which a black powder was obtained by

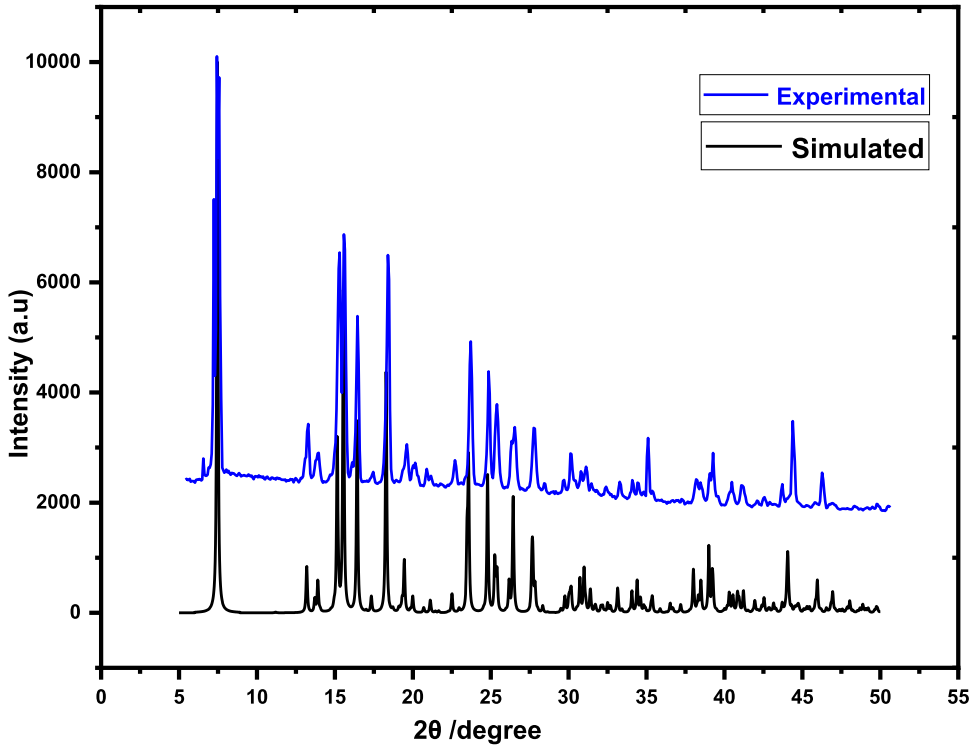

Fig. 1. Simulated and experimental powder XRD patterns of $[Cu_2(ox)(dien)_2](NO_3)_3$.

calcination. The formation of the nanocomposite was confirmed *via* powder X-ray diffraction (PXRD), Fourier Transform Infrared spectroscopy (FTIR) and Scanning Electron Microscopy (SEM).

2.3. Materials and methods

The μ-oxalato binuclear copper(II) complex was characterized by single-crystal X-ray diffraction, FTIR spectroscopy, Thermal Gravimetric analysis (TG-DSC) and UV–Visible spectrophotometry.

2.3.1. Single-crystal XRD

A suitable crystal, dimensions 0.17 × 0.13 × 0.04 (mm), was selected for X-ray diffraction analysis. Data were collected at room temperature using a Bruker D8 VENTURE diffractometer [using Mo-Kα radiation (λ= 0.71073 Å)], equipped with a Photon II CPAD detector and an IμS 3.0 (dual Cu and Mo) microfocus sealed tube generator. The diffraction data were collected and processed using *APEX3* (Ver. 2016.9–0 Bruker-AXS, 2016). The structure was solved using SHELXT [45] and refined using SHELXL [46] within OLEX2 [47]. All non-Hydrogen atoms were refined with anisotropic atomic displacement parameters. Hydrogen atoms were located in difference Fourier maps and refined freely. Crystal data collection and refinement details of the complex are summarized in Table 1. Atomic coordinates and basic geometrical data are reported respectively in Table 2 and Table 3, while the hydrogen bonds are given in Table 4. The CIF has been deposited with the Cambridge Structure Database CCDC 2,116,364. The structural graphics were created using the software Diamond [48].

2.3.2. X-ray powder diffraction

The phase purity of the studied compound was confirmed by powder XRD measurement (Fig. 1), the data were collected on a PANalytical X'Pert PRO X-ray powder diffractometer at room temperature using Cu Kα radiation (λ = 1.5418 Å). The 2θ scan range was 5–65° with a step size on 2θ of 0.067° The XRD pattern was

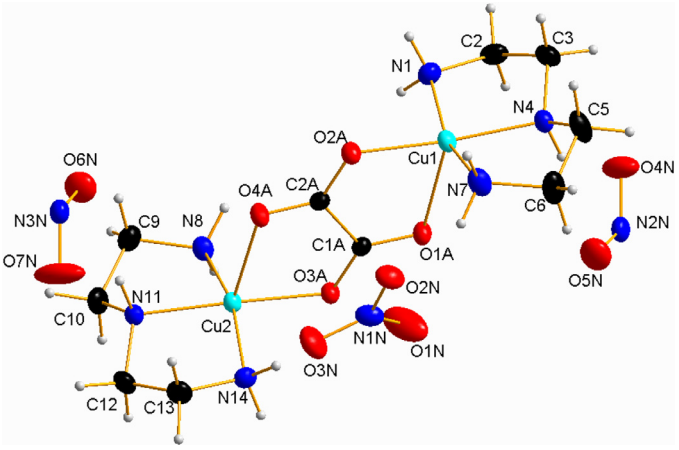

Fig. 2. Asymmetric unit in $[Cu_2(ox)(dien)_2](NO_3)_3$. Thermal ellipsoid plot at 50% probability level.

entirely consistent with the structure determined using the single-crystal XRD. A least square fit of the powder XRD lines (CuKα) using the (hkl) indices generated from single-crystal X-ray data, gave the cell parameters, which is in a good agreement with those determined by single-crystal XRD. Furthermore, their diffraction peaks are consistent with the simulated, indicating the purity of the as-synthesized product. The differences in intensities between the experimental and simulated XRPD patterns may be due to the variation in the preferred orientation of the powder sample during the collection of the experimental XRPD pattern [49].

2.3.3. IR spectroscopy

IR spectrum of the complex was recorded on a VERTEX 70 FTIR Spectrometer in the range 4000–400 cm^{-1} using the ATR technique at 4 cm^{-1} resolutions.

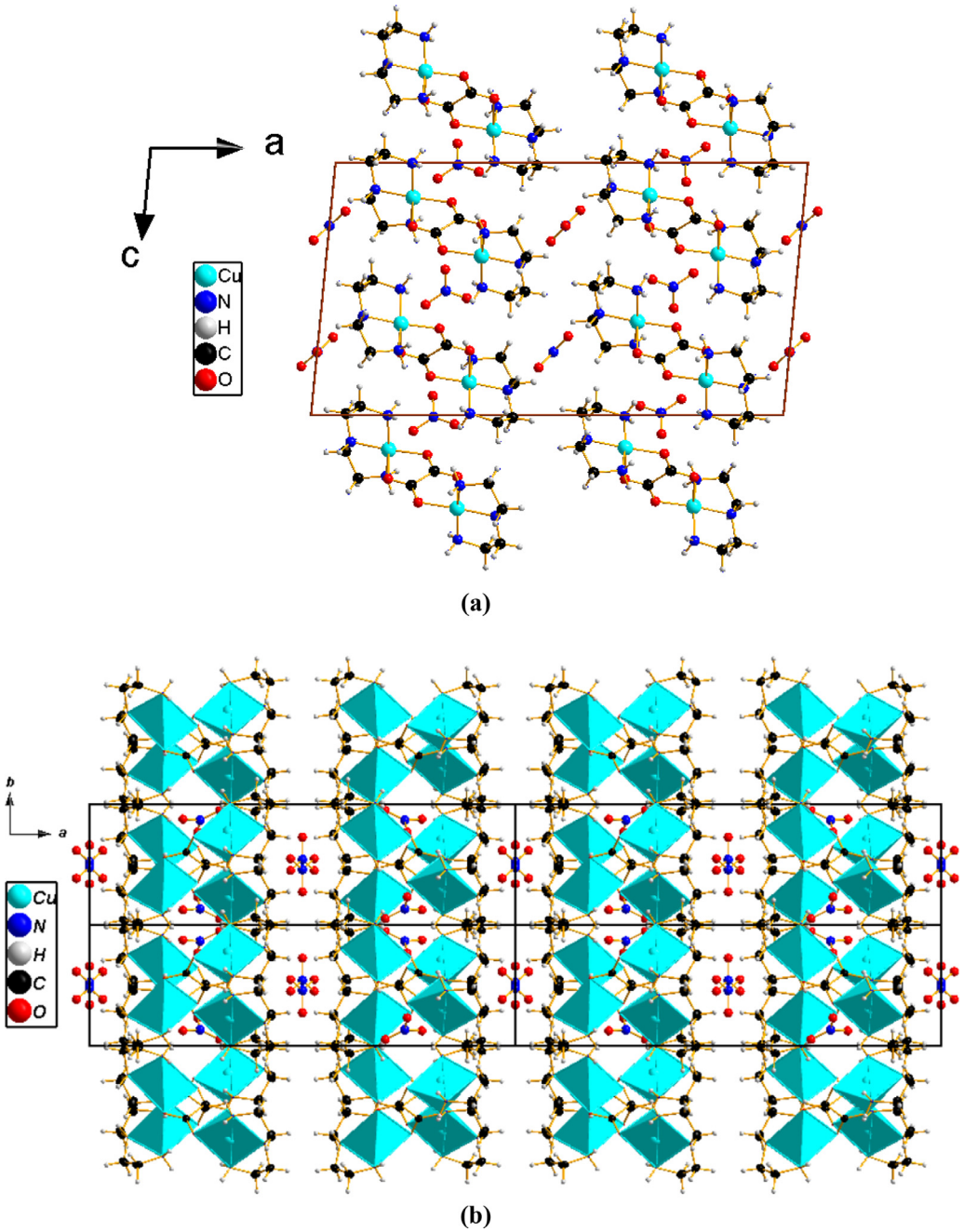

Fig. 3. (a) A view along *b* of the crystal structure of $[Cu_2(ox)(dien)_2](NO_3)_3$. (b) A projection along *c* of the studied complex polyhedrons.

2.3.4. UV–visible spectroscopy

UV–visible spectrum of the complex, which results from grounded crystals, was measured using a JASCO Scan Varian spectrophotometer in the range 200 - 900 nm.

2.3.5. TG-DSC analysis

TGA analysis was carried out on a Diamond TGA/DTA instrument (Perkin-Elmer) thermal analyzer (25–1000 °C) under nitrogen atmosphere, at a scan rate of 10 °C/min.

2.3.6. Magnetism measurements

The magnetic properties were measured on a Quantum Design MPMS system. The magnetization was measured as a function of applied magnetic field up to 20 kOe at 5 K and 300 K. The DC and AC magnetization and the ac susceptibility were measured as a function of temperature between 5 K and 300 K, in 5 K steps at an applied field of 100 Oe and ac frequencies of 10, 100 and 1000 Hz. Two temperature data sets were recorded: zero-field cooled, where the sample was initially cooled down under zero-field and field cooled, where the sample was cooled down under a field of 100 Oe.

2.3.7. DPPH radical scavenging activity

The antioxidant activity of $[Cu_2(ox)(dien)_2](NO_3)_3$ complex was evaluated using the test of 1–1 diphenyl-2-picrylhydrazyl (DPPH) free radical scavenging activity [50]. The hydrogen atom donating ability of the complex was measured from the bleaching of the purple-colored methanol solution of DPPH. 100 µL of various concentrations of the complex in methanol were added to 3.9 mL of the methanol solution of DPPH (1.01×10^{-2} M). After 30 min of incubation at room temperature, the absorbance was measured at

Table 3
Geometric parameters (Å, º) for $[Cu_2(ox)(dien)_2](NO_3)_3$.

Cu1—N1	2.007 (2)	N14—C13	1.485 (3)
Cu1—N4	1.993 (2)	C2—C3	1.508 (4)
Cu1—N7	2.003 (2)	C5—C6	1.510 (4)
Cu1—O1A	2.2409 (17)	C9—C10	1.516 (4)
Cu1—O2A	1.9770 (16)	C12—C13	1.511 (3)
Cu2—N8	2.004 (2)	O1A—C1A	1.242 (3)
Cu2—N11	1.9946 (19)	O2A—C2A	1.264 (3)
Cu2—N14	2.004 (2)	O3A—C1A	1.260 (3)
Cu2—O3A	1.9963 (16)	O4A—C2A	1.233 (3)
Cu2—O4A	2.2411 (16)	C1A—C2A	1.570 (3)
N1—C2	1.486 (3)	O1N—N1N	1.237 (3)
N4—C3	1.474 (3)	O2N—N1N	1.261 (3)
N4—C5	1.480 (3)	O3N—N1N	1.241 (3)
N7—C6	1.473 (3)	O4N—N2N	1.238 (4)
N8—C9	1.477 (3)	O5N—N2N	1.242 (2)
N11—C10	1.472 (3)	O6N—N3N	1.240 (2)
N11—C12	1.475 (3)	O7N—N3N	1.239 (4)
N1—Cu1—O1A	97.08 (8)	C13—N14—Cu2	108.31 (15)
N4—Cu1—N1	84.84 (8)	N1—C2—C3	107.8 (2)
N4—Cu1—N7	85.14 (8)	N4—C3—C2	107.5 (2)
N4—Cu1—O1A	106.32 (7)	N4—C5—C6	107.3 (2)
N7—Cu1—N1	161.03 (9)	N7—C6—C5	108.1 (2)
N7—Cu1—O1A	101.18 (8)	N8—C9—C10	108.2 (2)
O2A—Cu1—N1	95.02 (8)	N11—C10—C9	107.4 (2)
O2A—Cu1—N4	174.13 (8)	N11—C12—C13	107.2 (2)
O2A—Cu1—N7	93.32 (8)	N14—C13—C12	108.27 (19)
O2A—Cu1—O1A	79.54 (6)	C1A—O1A—Cu1	108.96 (14)
N8—Cu2—N14	162.30 (9)	C2A—O2A—Cu1	117.48 (15)
N8—Cu2—O4A	97.29 (8)	C1A—O3A—Cu2	116.48 (14)
N11—Cu2—N8	85.06 (8)	C2A—O4A—Cu2	108.94 (14)
N11—Cu2—N14	85.59 (8)	O1A—C1A—O3A	125.5 (2)
N11—Cu2—O3A	176.72 (7)	O1A—C1A—C2A	117.6 (2)
N11—Cu2—O4A	103.53 (7)	O3A—C1A—C2A	116.9 (2)
N14—Cu2—O4A	99.50 (8)	O2A—C2A—C1A	116.3 (2)
O3A—Cu2—N8	93.68 (7)	O4A—C2A—O2A	125.7 (2)
O3A—Cu2—N14	94.84 (8)	O4A—C2A—C1A	118.0 (2)
O3A—Cu2—O4A	79.62 (6)	O1N—N1N—O2N	119.1 (2)
C2—N1—Cu1	109.49 (15)	O1N—N1N—O3N	121.0 (2)
C3—N4—Cu1	108.07 (15)	O3N—N1N—O2N	119.9 (2)
C3—N4—C5	115.9 (2)	O4N—N2N—O5N	119.00 (18)
C5—N4—Cu1	108.25 (15)	O4N—N2N—O5N^{i}	119.00 (18)
C6—N7—Cu1	108.96 (15)	O5N^{i}—N2N—O5N	122.0 (4)
C9—N8—Cu2	109.27 (15)	O6N—N3N—O6N^{ii}	121.9 (3)
C10—N11—Cu2	108.18 (15)	O7N—N3N—O6N	119.06 (17)
C10—N11—C12	116.3 (2)	O7N—N3N—O6N^{ii}	119.06 (17)
C12—N11—Cu2	107.63 (15)		

Symmetry codes: (i) -*x* + 2, *y*, -*z* + 3/2; (ii) -*x* + 1, *y*, -*z* + 3/2.

Table 4
Hydrogen-bonds geometry (Å, º) for $[Cu_2(ox)(dien)_2](NO_3)_3$.

D—H···A	D—H	H···A	D···A	D—H···A
N1—H1*A*···O2*N*^{iii}	0.91	2.19	3.047 (3)	157
N1—H1*B*···O3*A*^{iv}	0.91	2.56	3.173 (3)	125
N1—H1*B*···O1*N*^{iv}	0.91	2.31	3.015 (3)	134
N4—H4···O4*N*	1.00	2.17	3.013 (2)	141
N4—H4···O5*N*	1.00	2.15	3.103 (3)	158
N4—H4···N2*N*	1.00	2.50	3.493 (3)	170
N7—H7*A*···O1*A*^{v}	0.91	2.56	3.219 (3)	130
N7—H7*A*···O3*A*^{v}	0.91	2.27	3.163 (3)	166
N7—H7*B*···O1*N*	0.91	2.28	3.184 (3)	170
N7—H7*B*···O2*N*	0.91	2.54	3.238 (3)	134
N8—H8*A*···O2*N*^{iii}	0.91	2.24	3.113 (3)	161
N8—H8*A*···N1*N*^{iii}	0.91	2.66	3.507 (3)	155
N8—H8*B*···O2*A*^{iii}	0.91	2.17	3.025 (3)	156
N11—H11···O6*N*	1.00	2.12	3.058 (3)	155
N11—H11···O7*N*	1.00	2.21	3.049 (2)	140
N11—H11···N3*N*	1.00	2.50	3.485 (3)	167
N14—H14*A*···O2*N*^{vi}	0.91	2.27	3.098 (3)	152
N14—H14*B*···O3*N*	0.91	2.28	3.129 (3)	156
C2—H2*A*···O1*A*^{iv}	0.99	2.64	3.422 (3)	136
C5—H5*B*···O5*N*^{vii}	0.99	2.62	3.345 (3)	131
C13—H13*B*···O6*N*^{viii}	0.99	2.56	3.283 (3)	130

Symmetry codes: (iii) *x*, -*y* + 1, *z*-1/2 ; (iv) *x*, *y* + 1, *z* ; (v) *x*, -*y* + 1, *z* + 1/2 ; (vi) *x*, -*y*, *z*-1/2.
(vii) -*x* + 2, -*y* + 1, -*z* + 2 ; (viii) *x*, *y*-1, *z*.

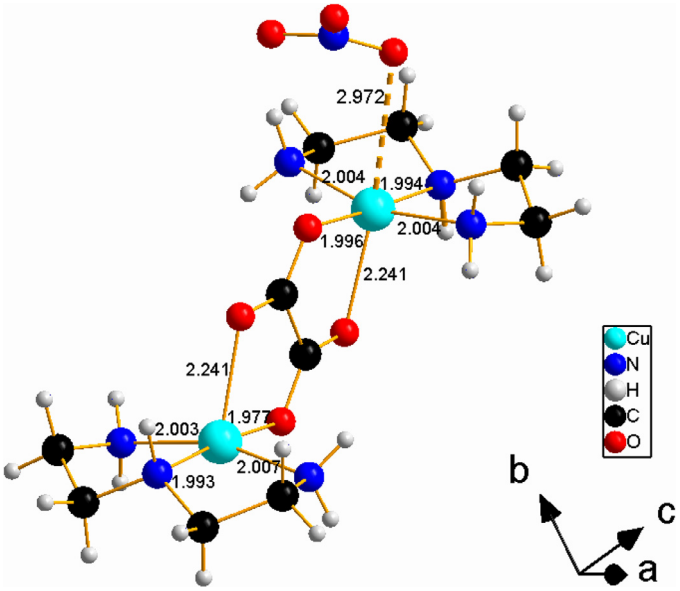

Fig. 4. Jahn-Teller distortion acting on Cu2 to give rise to the octahedral (5 + 1) coordination $[Cu2O_{5+1}]$.

517 nm. Butylhydroxytoluene (BHT) was used as the standard. The percentage of DPPH scavenging activity (% inhibition) was calculated using the equation as given below:

$$\%inhibition\ of\ DPPH = \left(\frac{A_b - A_s}{A_b}\right) \times 100$$

where, A_b is the absorbance of the blank (solvent without sample) and A_s is the absorbance of the sample and the positive control. The sample concentration providing 50% inhibition (IC_{50}) of DPPH free radical was calculated from the graph plotting% inhibition against sample concentration. Tests were carried out in triplicate.

2.3.8. Ferric reducing antioxidant power (FRAP assay)

In this test, the antioxidant activity is measured by the ability of the $[Cu_2(ox)(dien)_2](NO_3)_3$ complex to transfer a single electron to reduce Fe^{3+} to Fe^{2+} [51]. Different concentrations of the sample were mixed with 2.5 mL of phosphate buffer (0.2 M, pH 6.6) and 2.5 mL of 1% potassium ferricyanide $[K_3Fe(CN)_6]$. The mixture was incubated at 50 °C for 20 min. 2.5 mL of trichloroacetic acid (10%) were added and the mixture was centrifuged. The upper layer of solution (2.5 mL) was mixed with 2.5 mL of distilled water and 0.5 mL of 0.1% $FeCl_3$. The absorbance was measured at 700 nm using a UV–Visible spectrophotometer against a blank (solvent without sample) and gallic acid was used as the standard.

2.3.9. Phosphomolybdenum assay

The total antioxidant capacity was measured using the test of Phosphomolybdenum as described by [52]. The method is based on the reduction of Mo (VI) to Mo(V) by the studied compound and the formation of a green phosphate-Mo(V) complex at acidic pH. Briefly, 0.3 mL of the sample with various concentrations was added to 3 mL of the reagent (0.6 M sulfuric acid, 28 mM sodium phosphate and 4 mM ammonium molybdate). The mixture was incubated in 95 °C for 90 min. Absorbance readings were recorded at 695 nm against a blank using a UV–Visible spectrophotometer. The TAC of the sample was expressed as (µg/mL) ascorbic acid equivalent and gallic acid was used as the standard.

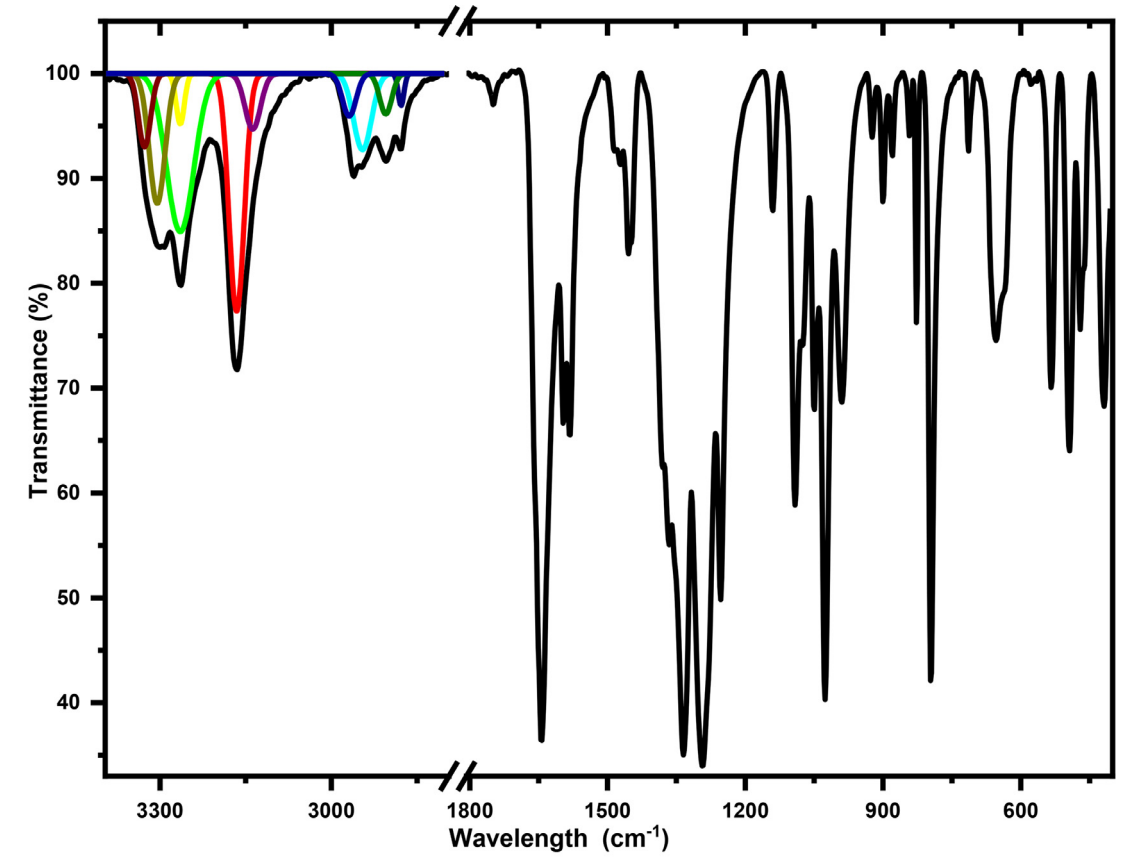

(a)

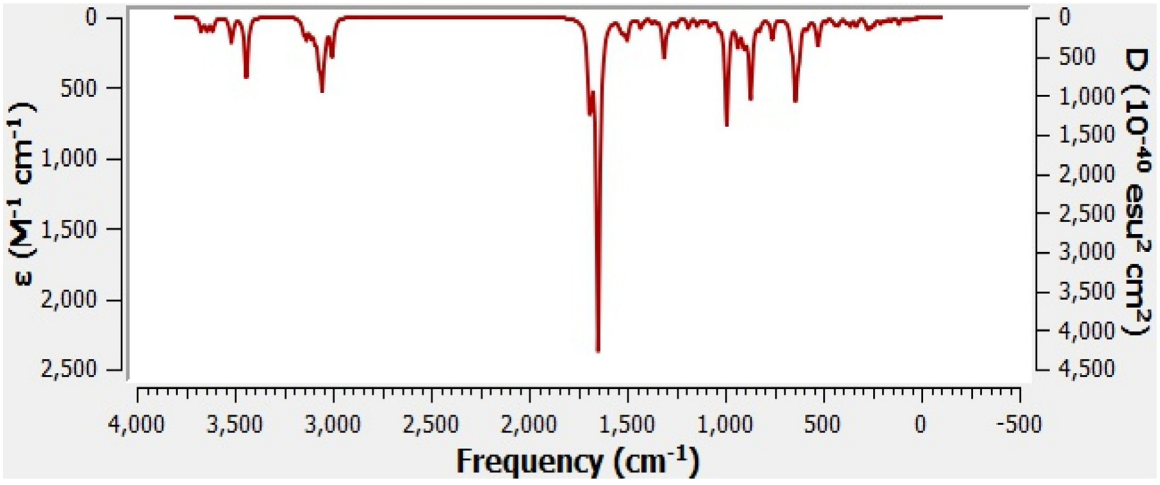

(b)

Fig. 5. (a) Experimental and (b) calculated Infrared spectra of $[Cu_2(ox)(dien)_2](NO_3)_3$.

2.3.10. Characterization of CuO nanoparticles

Powder X-ray diffraction (PXRD) was utilized to record the patterns in the range of 05–80° in 2θ utilizing a PANalytical XPERT-PRO diffractometer with Cu-K_α radiation (λ_{Cu}= 1.54060 Å). The average size of particles (by suggesting that the particles are spherical) was estimated from Scherer's equation ($D = \frac{k\lambda}{\beta \cos\theta}$), where β is the width of the observed diffraction peak at its half maximum intensity (FWHM) expressed in radians, K is the shape factor, which takes a value of about 0.9, λ is the X-ray wavelength (CuK_α radiation, equals to 0.15060 nm) and θ is the Bragg angle [53].

2.3.11. Theoretical calculations' details

All the theoretical calculations of the title complex were performed with the program Gaussian [54,55] at the M06–2X/LANL2DZ level in water, by optimizing its structure, finding the contour plots of the frontier molecular orbitals FMOs and the

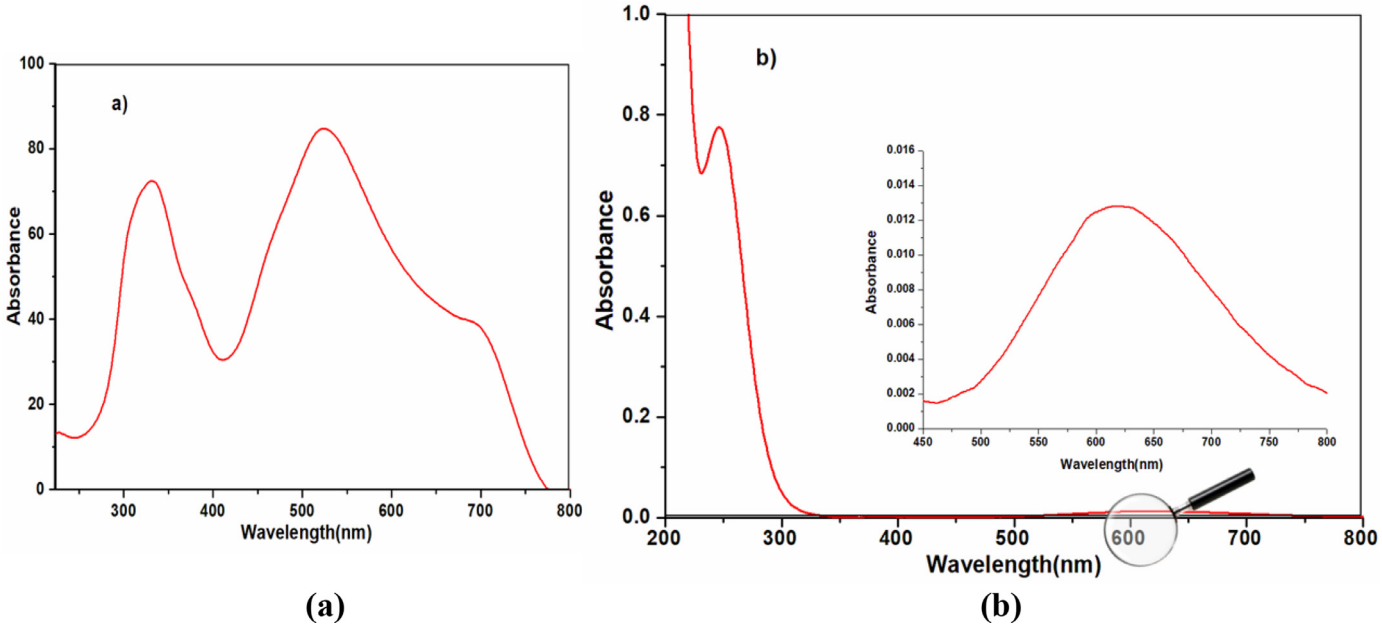

Fig. 6. UV-visible spectra of $[Cu_2(C_2O_4)(C_4H_{13}N_3)_2](NO_3)_3$ complex (a) in solid state and (b) in water (10^{-4} M) at room temperature.

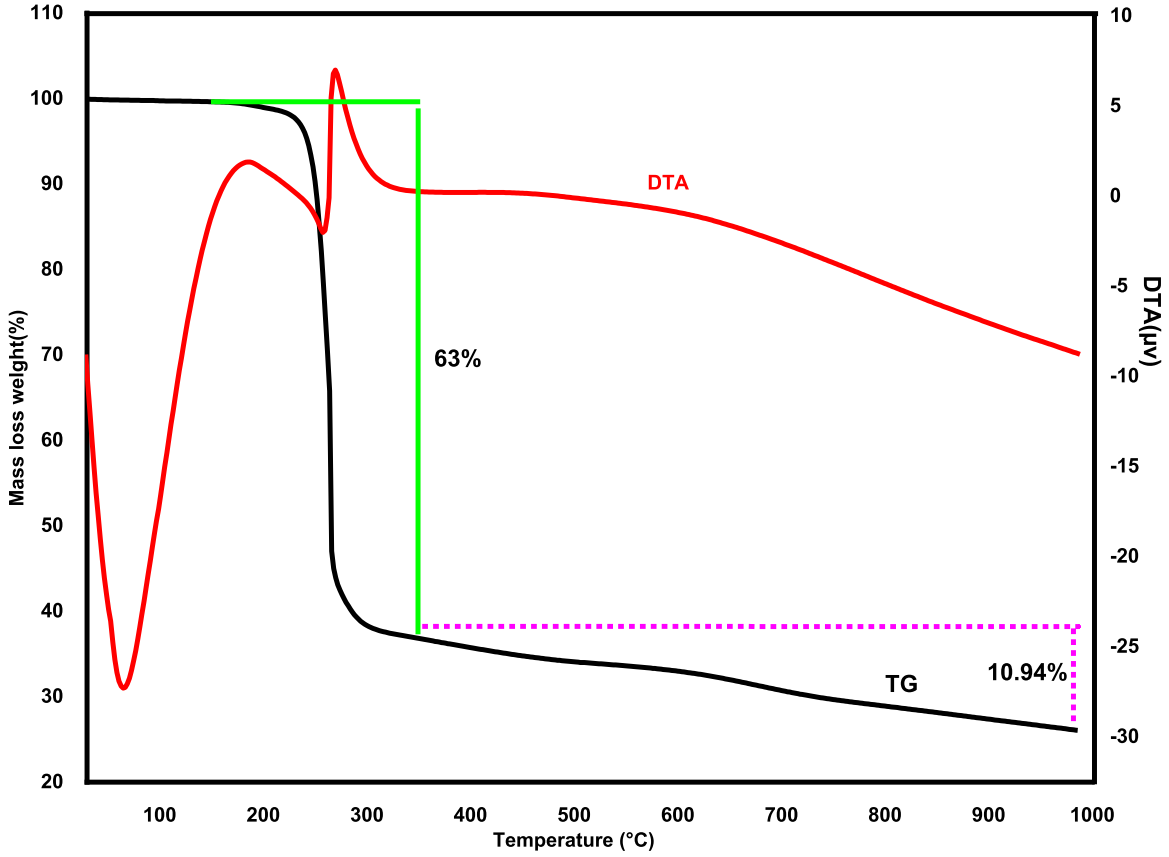

Fig. 7. DTA/TG and DTGA curves of $[Cu_2(ox)(dien)_2](NO_3)_3$.

molecular electrostatic potential MEP maps. Moreover, the IR spectrum of the studied complex was computed in the range 500–3500 cm^{-1}.

2.3.12. Hirshfeld *surface analysis HSA*

In order to gain insights into the leading stabilizing contacts and interactions in the title complex, it was examined in terms of its molecular packing by carrying out *Hirshfeld* surface HS and 2D Fingerprint plot FP analyses using the program CrystalExplorer17.5 [56]. The HSs of the complex were mapped over the following functions: d_{norm}, d_i and *shape index*, in the respective ranges [−0.4054, 1.4999] Å, [0.8638, 2.3112] Å and [−0.9961, 0.9972] Å.

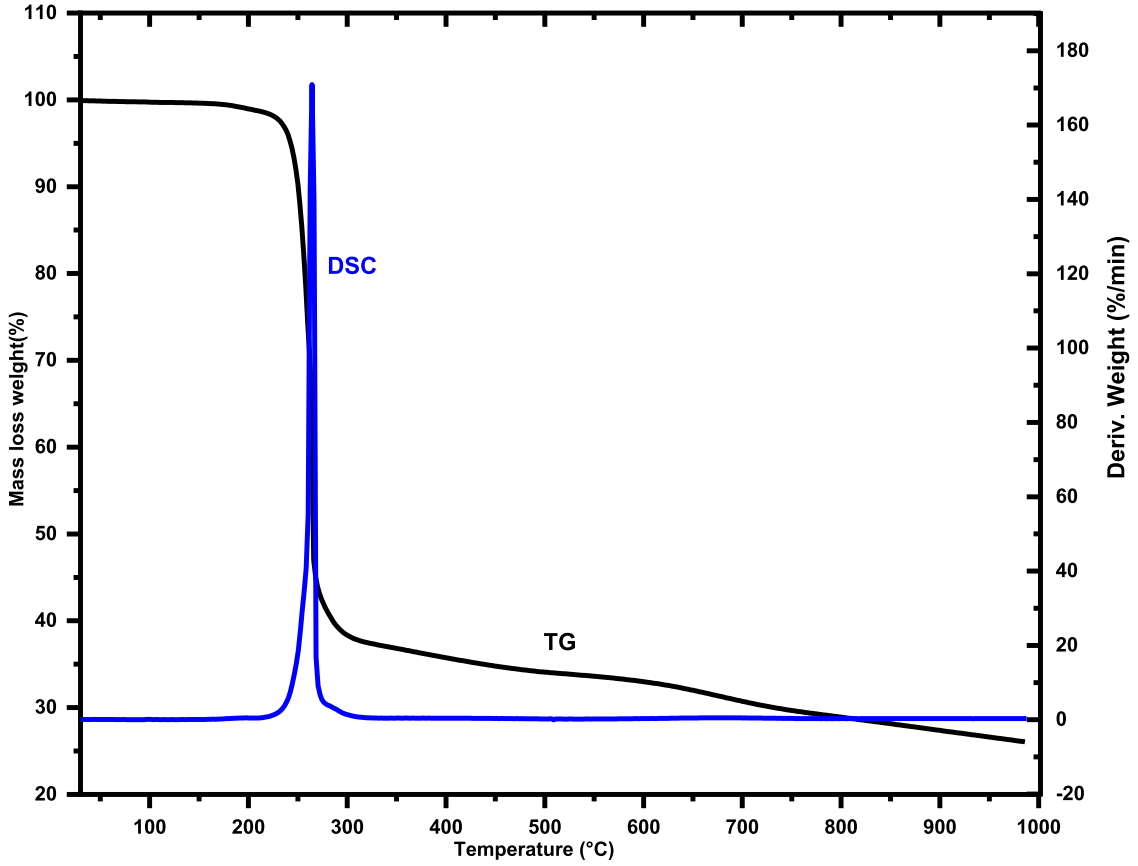

Fig. 8. DSC curve of $[Cu_2(ox)(dien)_2](NO_3)_3$.

2.3.13. Topological analysis

The topological underlying nets discussed in this manuscript were obtained using the software package ToposPro [57], in order to simplify the description of the title complex's molecular network for a better understanding of the oxalato-bridged copper(II) frameworks.

3. Results and discussion

3.1. Structural study

The asymmetric unit (Fig. 2) contains two independent $[Cu(C_2O_4)(dien)]$ units, sharing the oxalate-bridge to build up the dimmer $[Cu_2(C_2O_4)(dien)_2]^{2+}$, and three non-coordinated nitrate (NO_3^-) ions. Selected bond lengths and angles are given in Table 3. The Cu^{2+} ions (Cu1 and Cu2) sit in two general positions.

The cation Cu1 is five-coordinated by three nitrogen atoms and two oxygens $[Cu1N_3O_2]$, where the diethylenetriamine group acts as a facially coordinated tridentate ligand, while the oxalate anion bonds to the metallic center by acting as a bidentate ligand. At first insight, the second metallic cation Cu2 is similarly coordinated. In this case, the coordination polyhedrons $[Cu2N_3O_2]$, close to square pyramidal (Figs. 3a and 3b), are quantitatively characterized using the parameter τ defined by Addison et al. [58,59]. The calculated values are $\tau = 0.218$ for Cu1 and $\tau = 0.240$ for Cu2. There is no explanation for the difference in τ for Cu1 and Cu2; however, considering the Jahn-Teller effect in the case of Cu^{+2} with a $3d^9$ electronic configuration, with one unpaired electron, seems to occur especially for Cu2 as depicted in Fig. 4.

The distortion of Cu2 rises, resulting in a hexa-coordinated $[Cu2N_3O_3]$ octahedron, with a long Cu2-O3N bond distance of 2.972 Å. Indeed, in this case, a further distortion can be expressed by the "mean quadratic elongation" [60,61]; wherein the bond length distortion is defined as $\Delta oct = \frac{1}{6}\Sigma([R_i-\bar{R}]/\bar{R})2$ (R_i is the individual bond length and $\bar{R}$ is the average bond length). This parameter is calculated to be $\Delta oct = 0.125$ and indicates a very strong distortion of CuN3O3 octahedron. The Cu1–Cu2 distance across the oxalate is 5.464 Å, which is significantly shorter than the similar distance reported in other oxalato-bridged copper (II) complexes, being 5.931(3) Å [13]. Therefore, it is found in dinuclear copper(II) complexes in which the oxalato ligand bridges are in asymmetrical bis-bidentate coordination between the two metal centers [62].

3.2. Infrared spectroscopy

The experimental and theoretical spectra of the studied compound are given in Figs. 5a and 5b, respectively. The experimental spectrum (Fig. 5) exhibits characteristic vibrational bands of ligated moieties and free nitrate anions. Thus, the strong broad absorption centered with three shoulders at 1360, 1334 and 1296 cm^{-1} is assigned to the asymmetric stretching vibration (ν_3) of the nitrate anions. Similarly, this mode of vibration appears approximately at 1311.10 cm^{-1} in the calculated spectrum (Fig. 5). While, the set of bands, appearing at around (820 and 790 cm^{-1}) in the experimental spectrum and at (800 and 710 cm^{-1}) in the computed one, could be associated to the in plane (ν_2) and out of plane (ν_4) deformations of the non-coordinated nitrate, respectively. Moreover, the presence of a weak absorption around 1050 cm^{-1} in the experimental spectrum (and at around 1010 cm^{-1} in the theoretical one) confirms the involvement of the nitrate ions in a hydrogen bonding network [63]. On the other hand, the bands located at around 1720 and 1450 cm^{-1} are attributed to the asymmetric

Table 5
Bands assignments of electronic spectra of $[Cu_2(C_2O_4)(C_4H_{13}N_3)_2](NO_3)_3$ complex.

	λ_{max} (nm)	ε (l.mol^{-1}.cm^{-1})	σ (cm^{-1})	Transition
Solid state	332 526–692	- -	30,120 19,012–14,450	n–π^* d_{xy}, d_{yz} → $d_x{}^2{}_{-y}{}^2$
Water	249 550–700	7700 120	40,160 18,182–14,286	n–π^* d_{xy}, d_{yz} → $d_x{}^2{}_{-y}{}^2$

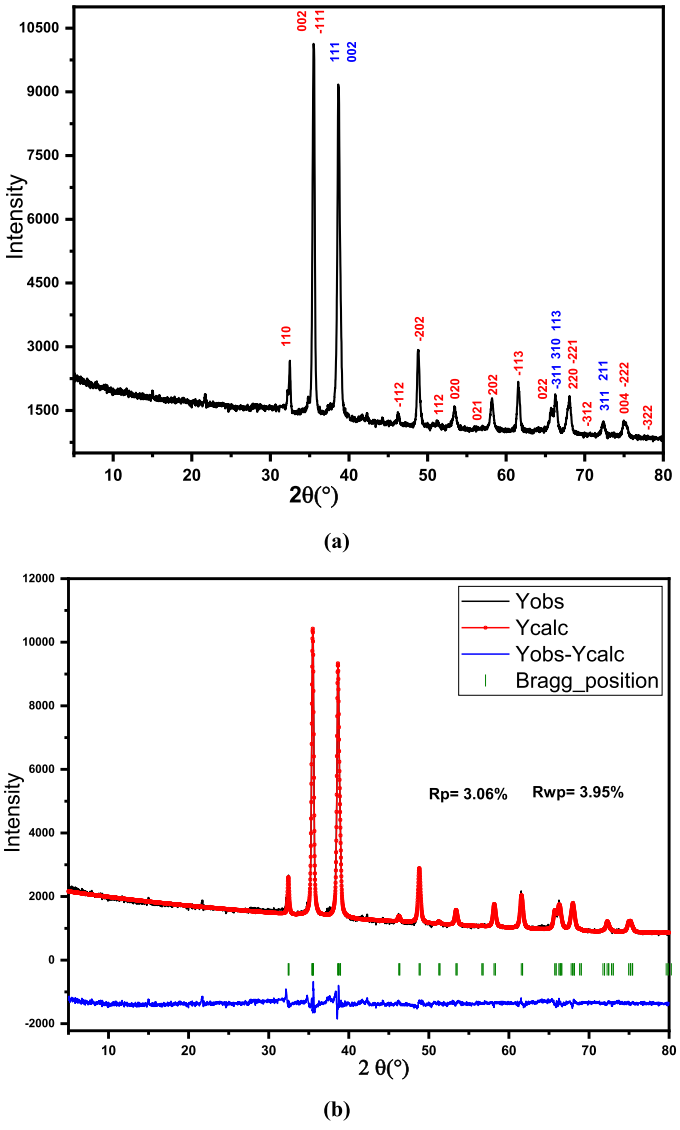

Fig. 9. (a) Indexation, (b) comparison between the experimental and calculated powder X-ray diffraction patterns of CuO–NPs. .

ν_{as}(C–O) and symmetric ν_s(C–O) stretching modes of the oxalato-bridging ligand. Correspondingly, these vibrations were calculated at 1647 and 1470 cm^{-1}, respectively. Whereas, the δ(O–C–O) bending mode, characteristic of the bischelating arrangement of the oxalate units, was observed at 869 and 820 cm^{-1} in the respective theoretical and experimental spectra. Therefore, the occurrence of the bischelating oxalate [11] is clearly reflected in these stretching and deformation vibrations. In addition, the bands at 3300 and 3140 cm^{-1} can be ascribed to the respective asymmetric ν_{as}(N–H) and symmetric ν_s(N–H) band stretching modes of the ($-NH_2$) group in the dien ligand. Similarly, these vibrational modes were manifested in the computed spectrum through the two bands appearing at 3517 and 3440 cm^{-1}. The weak absorption pointing out at 2800 cm^{-1} manifests the presence of ν($-CH_2$) stretching vibration of the methylene group, while its deformation mode appears at around 1480 cm^{-1} with a small shoulder. Correspondingly, the theoretical asymmetric ν_{as}($-CH_2$) and symmetric ν_s($-CH_2$) stretching modes of the methylene C–H bonds were computed at 3054 and 3004 cm^{-1}, respectively. As for the computed absorption band appearing at 1693 cm^{-1}, it is related to the ligand's ν(C–C) and ν(C–N) stretching modes. Furthermore, the medium experimental vibrations located in the range 530–470 cm^{-1} and associated to the ν(Cu–N) and ν(Cu–O) stretching vibrations, they confirm the coordination of the oxalate and diethylenetriamine ligands [64,65]. This coordination is additionally reflected in the appearance of absorptions at 642 and 526 cm^{-1} in the computed spectrum.

3.3. Electronic spectroscopy

The electronic spectrum of the $Cu_2(C_2O_4)(C_4H_{13}N_3)_2(NO_3)_3$ complex was recorded in water solution (10^{-4} M) at room temperature and in solid state for the wavelength range 200–1000 nm. The relevant electronic spectral data are summarized in Table 5. Representative spectra of the complex are displayed in Fig. 6. In solid state, the absorption spectrum of the Cu(II) complex showed an intense band at 332 nm, which could be assigned to the n–π^* transition of the (C = O) group arising from the oxalate moiety, which relates to the absorption band appearing at 19,012 cm^{-1} with a broad shoulder at 14,450 cm^{-1}. These spectral features are typical of five-coordinate Cu(II) complexes and expected for the square pyramidal (SP) geometry, where the absorption band results from d_{xy}, d_{yz} → $d_x{}^2{}_{-y}{}^2$ transition [66,67]. The obtained geometry is in agreement with the single-crystal results, where both Cu(II) metallic centers are five-coordinated as square pyramidal polyhedrons. In water solution, the complex shows a board bond with a molar extinction coefficient of 120 L.mol^{-1}.cm^{-1} around 18,182–14,286 cm^{-1}, similarly to the results observed in the solid state. The shifts observed in water solution are minor and may be due to the slight distortion of the geometry. We also noticed, that the absorption band corresponding to the n–π^* transition is blue shifted to 249 nm in water solution.

3.4. Thermal analysis

Thermal stability of $[Cu_2(C_2O_4)(C_4H_{13}N_3)_2](NO_3)_3$ was performed under nitrogen flow. As depicted in Fig. 7, the experimental profile shows thermal resistance of the copper oxalate material until 200 °C, followed by two cleanly separated stages of weight loss in total of 73.94%. The first theoretical mass loss (63%), occurring between 200 and 346 °C, corresponds to the total volatilization of the organic ligands and the nitrate units. The sharp weight loss also coincides with the start decomposition of the bis-chelating oxalate as carbon oxide. This mass loss is in agreement with the calculated value of 63.12%.

Furthermore, this variation is coupled with an exothermic intense peak of DSC curve (Fig. 8) and with an endothermic signal in the DTA trace, pointing at 250 and 260 °C, respectively. The final weight loss of 10.94%, extending between 350 and 950 °C, is attributed to the slower and total degradation of the remaining oxalate bridging ligands into copper oxide as a final product with a matched calculated value of 10.63%. This final variation is charac-

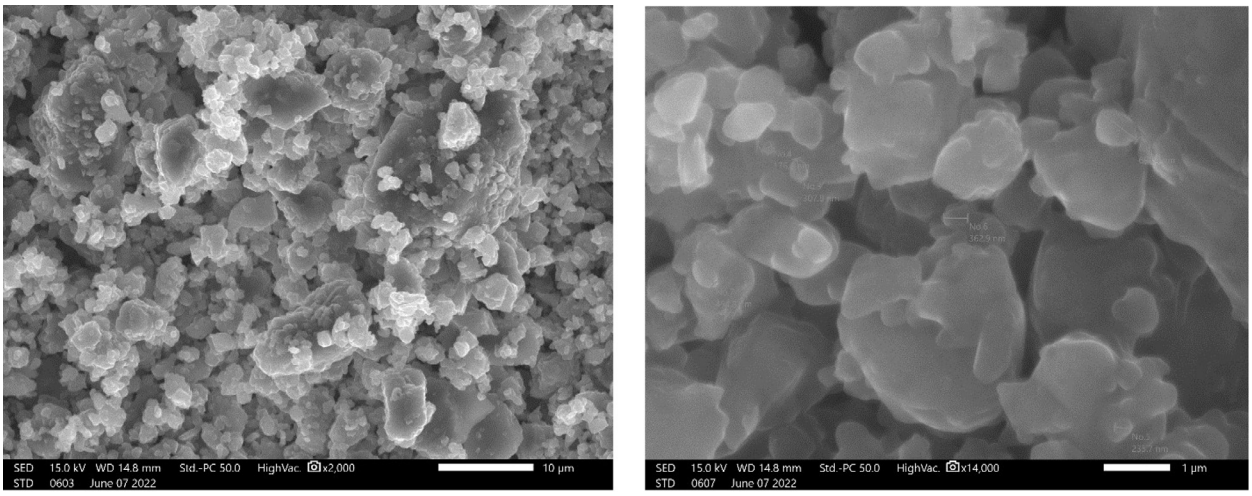

Fig. 10. Scanning Electron Microscope micrographs of (a) the studied complex $[Cu_2(ox)(dien)_2](NO_3)_3$ and (b) the resulting CuO nanoparticles.

terized by none heat flow curves in both DTA and DSC measurements. The thermal decomposition can be systematized by the following equations:

$$[Cu_2(C_2O_4)(C_4H_{13}N_3)_2](NO_3)_3 \xrightarrow{\Delta} Cu_2(CO_3) + (C_4H_{13}N_3)_2 + 3NO_{3(g)} + CO_{(g)}$$

$$Cu_2(CO_3) \xrightarrow{\Delta} Cu_2O + CO_{(g)} + CO_{2(g)}$$

3.5. Study of the CuO nanoparticles

Fig. 9 depicts the XRD pattern acquired after calcination of the precursor at 725 °C. Average size of the particles is around 23.33 nm. The particles size of each sample consists of significantly agglomerated spherical nanoparticle with diameters of about 19.30–25.50 nm assembled within agglomerates of about 1–10 µm, which is clearly visible in the SEM image (Figs. 10a and 10b). However, this size is not confirmed by X-ray diffraction analysis.

The smaller value (23.33 nm) from XRD analysis can be explained by the fact that XRD determines the crystallite size and not the particle size. Agglomeration of the crystallites results in the formation of particles of greater size. As a result, there will be less adsorption of nitrogen molecules in the case of an agglomerated powder.

FTIR spectra of CuO–Nanoparticles (NPs) are presented in Fig. 11. In the IR spectrum of the calcined product, the elimination of vibration bands of the organic amine and the nitrate anions is observed. In fact, the three absorption bands that appeared at 460, 530 and 589 cm^{-1} are correlated with Cu(II)-O stretching vibrations confirming the formation of CuO NPs [43,44]. Moreover, the strong broad absorption band that appeared at 950–1050 cm^{-1} may be associated with the C–C stretching and the O–H bending vibrations. Based on the XRD pattern of the calcination product shown in Fig. 9a, the copper coordination complex lead to the simultaneous formation of CuO nanoparticles [68,69]. The formation of metallic Cu may be due to the reduction of a trace amount of the Cu(II) ions surrounded by the coordinated organic ligands or nitrate counter ions in the complex. Bragg's reflections located at

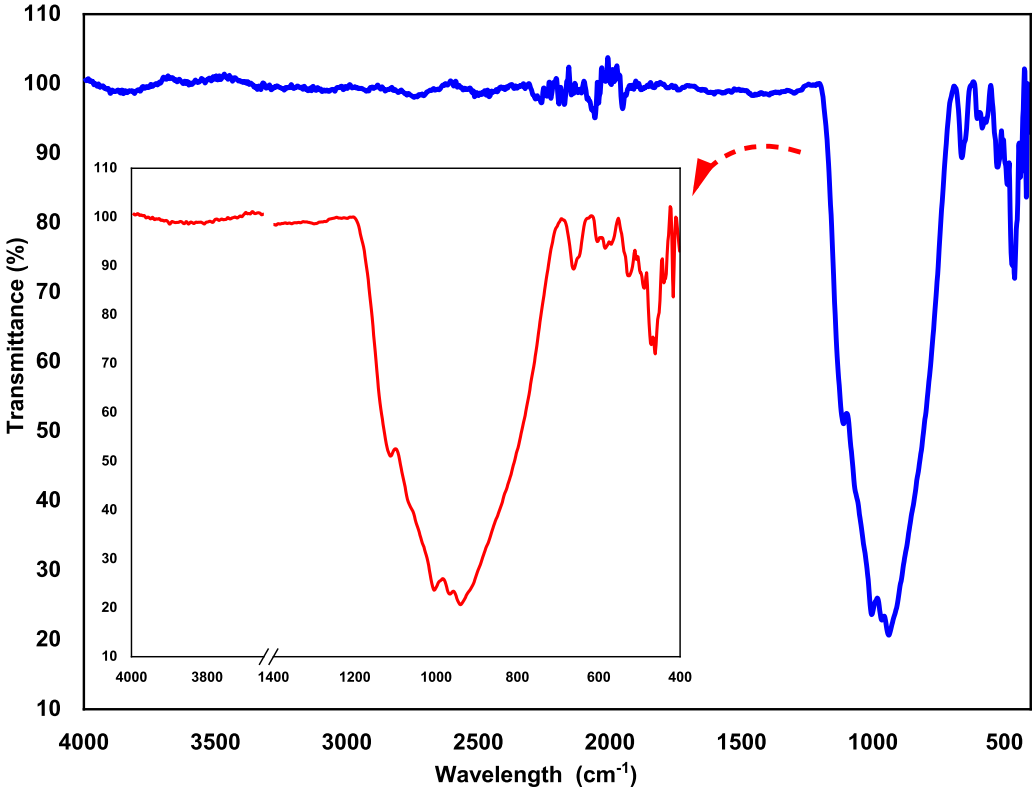

Fig. 11. FTIR spectrum of the CuO nanoparticles.

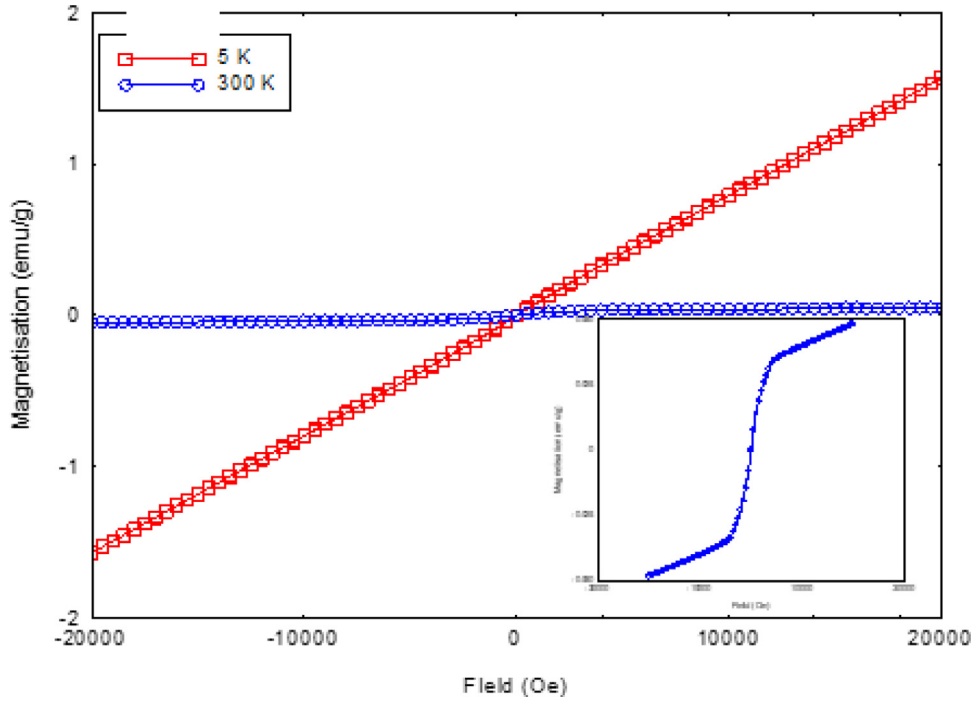

Fig. 12. Magnetization as a function of magnetic field at 5 K and 300 K, inset: at 300 K.

about 2θ values of 32.488, 35.434, 35.550, 38.667, 38.947, 46.282, 48.841, 51.284, 53.396, 56.634, 58.206, 61.576, 65.728, 66.303, 66.486, 67.819, 68.036, 68.867, 71.807, 72.336, 72.849, 74.982, 75.260 and 79.657° belong to the lattice planes of (110), (002), (−111), (111), (200), (−112), (−202), (112), (020), (021), (202), (13), (022), (−111), (310), (113), (220), (−221), (−312), (311), (221), (004), (−322), and (023), respectively. Rietveld analysis of the PXRD pattern confirmed the sample quality, all reflection peaks corresponding to 2θ values were indexed in the monoclinic system with the C2/c space group with lattice parameters similar to those obtained from (JCPDS card no. 05–0661), as displayed in Fig. 9b. Only very minor peaks were observed from possible impurity phase(s) [70]. The CuO nanoparticles in our work were comparable to the ones prepared from $[Cu_2(2,2\text{-bpy})_2(Fc(COO)_2)](BF_4)_2.H_2O.3CH_3OH$

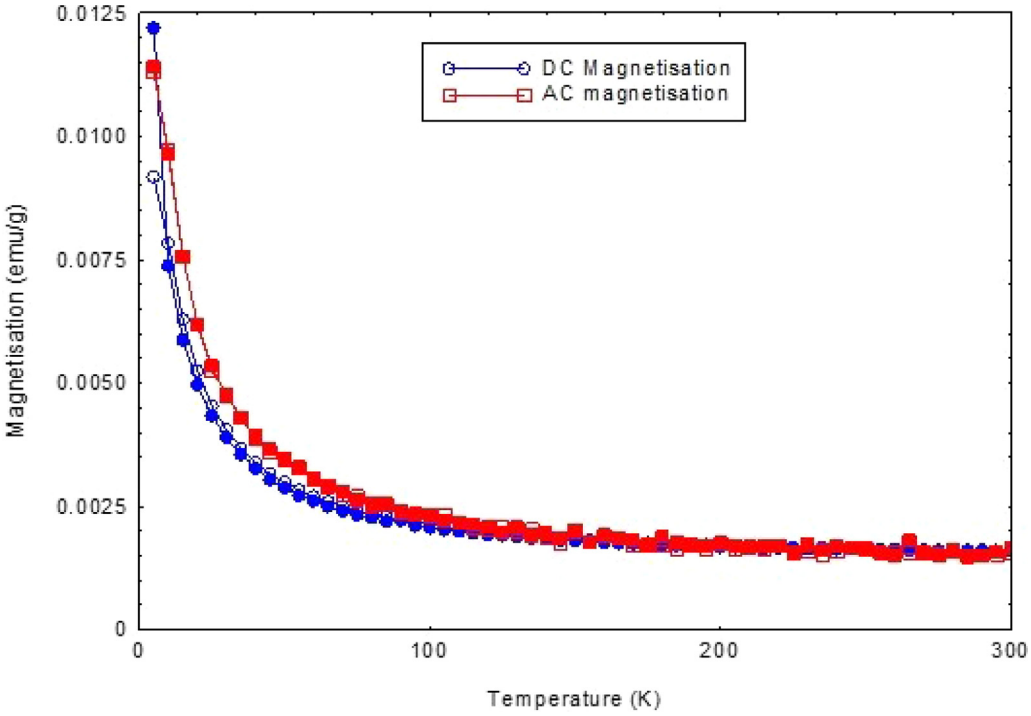

Fig. 13. DC and AC magnetization as a function of temperature, at an applied field of 100 Oe and 1000 Hz. The solid symbols represent the zero-field cooled data and the open symbols represent the field cooled data.

Table 6
Selected experimental and calculated geometric parameters around the metallic centers in complex $[Cu_2(ox)(dien)_2](NO_3)_3$ (Å, °).

	Experimental	Calculated		Experimental	Calculated
Bond distances					
Cu1—N1	2.007(2)	2.2746	Cu2—N14	2.004(2)	2.2747
Cu1—N4	1.993(2)	2.1026	Cu1—O1A	2.2409(17)	2.7025
Cu1—N7	2.003(2)	2.1998	Cu1—O2A	1.9770(16)	2.1044
Cu2—N8	2.004(2)	2.2001	Cu2—O3A	1.9963(16)	2.1045
Cu2—N11	1.9946(19)	2.1026	Cu2—O4A	2.2411(16)	2.7018
Bond angles					
N4—Cu1—N1	84.84(8)	71.9	N8—Cu2—N14	162.30(9)	136.3
N4—Cu1—N7	85.14(8)	71.3	N11—Cu2—N8	85.06(8)	71.3
N7—Cu1—N1	161.03(9)	136.3	N11—Cu2—N14	85.59(8)	72.0
N1—Cu1—O1A	97.08(8)	82.8	N8—Cu2—O4A	97.29(8)	82.8
N4—Cu1—O1A	106.32(7)	134.6	N11—Cu2—O3A	176.72(7)	142.8
N7—Cu1—O1A	101.18(8)	102.3	N11—Cu2—O4A	103.53(7)	134.6
O2A—Cu1—N1	95.02(8)	82.8	N14—Cu2—O4A	99.50(8)	102.4
O2A—Cu1—N4	174.13(8)	142.8	O3A—Cu2—N8	93.68(7)	80.3
O2A—Cu1—N7	93.32(8)	80.3	O3A—Cu2—N14	94.84(8)	82.8
O2A—Cu1—O1A	79.54(6)	69.4	O3A—Cu2—O4A	79.62(6)	69.5

complex [71]. The calculated crystalline sizes from Scherer's equation and based on the highest diffraction peak is about 19.30 and 25.50 nm for CuO–NPs, respectively. Figs. 10a and 10b show respectively the SEM images of the complex $[Cu_2(ox)(dien)_2](NO_3)_3$ and the CuO nanoparticles that have been formed as agglomerated particles.

3.6. Magnetic study

The results of the magnetic measurements are depicted in Fig. 12. It is observed that at room temperature (300 K), a hysteresis loop was measured, although paramagnetic or antiferromagnetic behavior was observed at 5 K. This suggests that there are two magnetic components within the sample, with the paramagnetic component dominating at low temperatures and the ferromagnetic component only being observed at higher temperatures. This is observed at 300 K, where at low fields the signature "s" shape of a ferromagnetic hysteresis loop is observed. While, at high fields, where the ferromagnetic phase has reached saturation, the paramagnetic linear dependence on magnetic field is observed. Due to both components occurring at 300 K, it is more difficult to determine the Curie constant of the paramagnetic phase from the data. The susceptibility can be determined from the gradient of the magnetization at fields higher than 10 kOe. Fitting a line to the data allowed obtaining the susceptibility, which was found to be 8.53×10^{-7} emu/g.Oe. The saturation magnetization of the ferromagnetic component is determined by subtracting the paramagnetic contribution away from the total magnetization, which gave a saturation magnetization of 0.031 emu/g. Thus, the paramagnetic contribution at 300 K and 20 kOe is 0.175 emu/g.

There is a slight difference between the DC and AC magnetization as a function of temperature, but both have an increase in

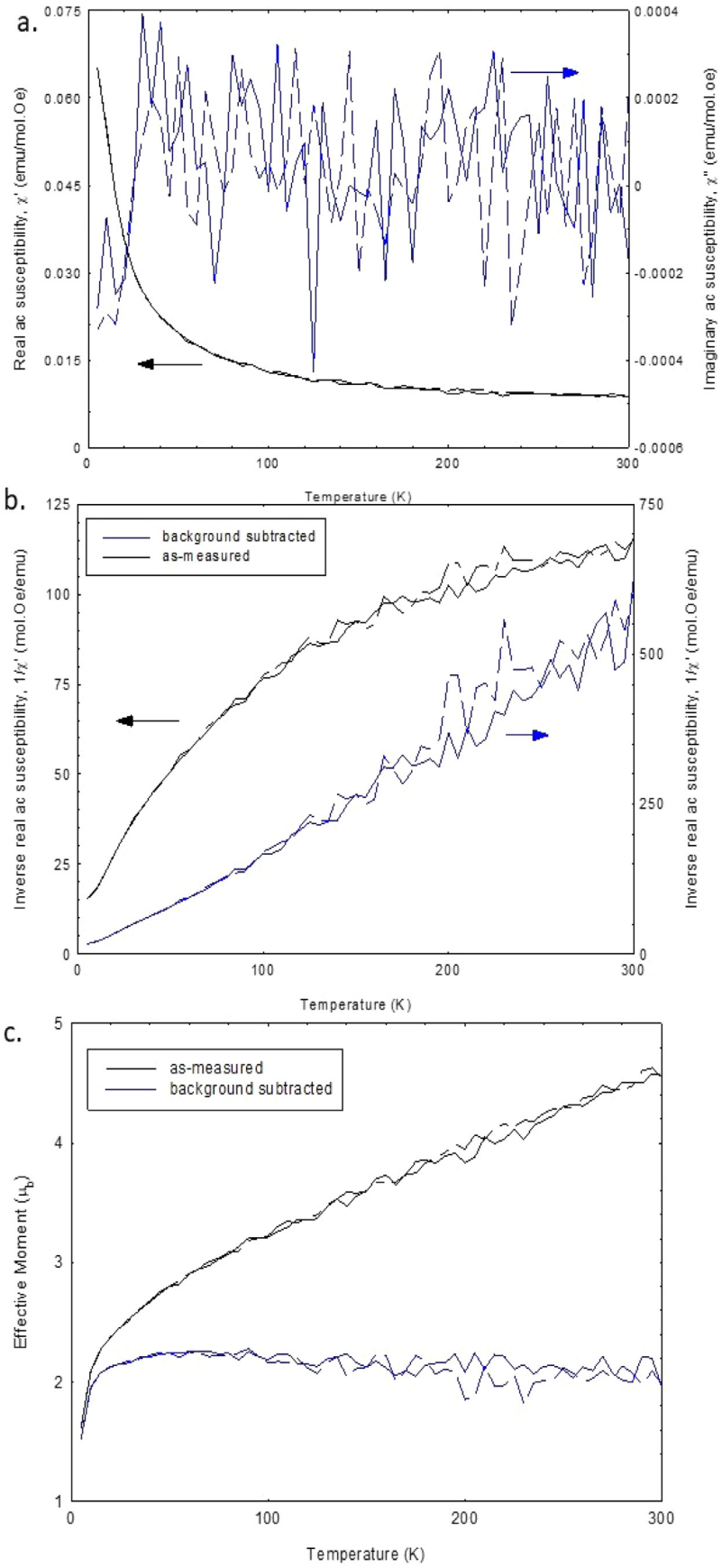

Fig. 14. (a) Real and Imaginary molar AC susceptibility as a function of temperature, for 100 Oe and 1000 Hz data only; (b) Inverse real molar AC susceptibility as a function of temperature for 1000 Hz, for as-measured and after the independent component (background) has been substracted; (c) Effective moment for both the as-measured data and the independent component (background) subtracted data as a function of temperature. The solid lines represent the zero-field cooled data and the dashed lines represent the field cooled data.

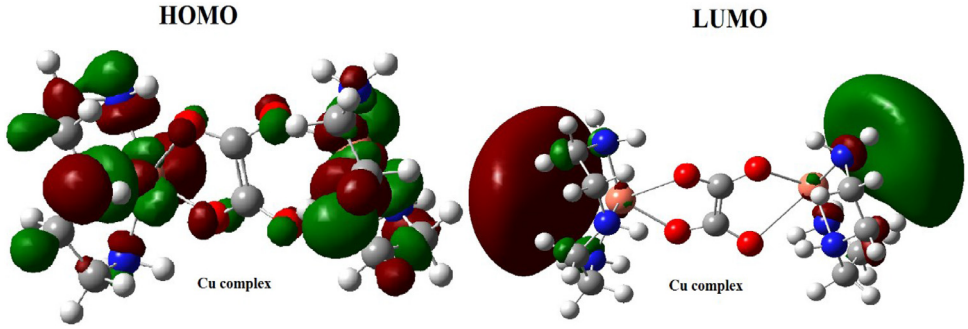

Fig. 15. Contour plots of the HOMO and LUMO molecular orbitals in complex $[Cu_2(ox)(dien)_2](NO_3)_3$.

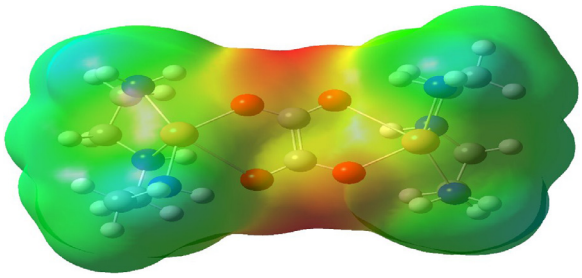

Fig. 16. Representation of the MEP map computed around the studied complex.

magnetization as the temperature is increased. There is also no difference between the field cooled and the zero-field data, suggesting that the 5 K magnetization state is paramagnetic rather than antiferromagnetic, as no peak is observed in the data where the transition between paramagnetic and antiferromagnetic occurs (Fig. 13).

The ac susceptibility data is given in Fig. 14, with only the 1000 Hz data presented, as the 10 and 100 Hz data were nosier with the same trends as the 1000 Hz. Although the real ac susceptibility part (Fig. 14a) looks similar to what would be expected for a paramagnetic/antiferromagnetic compound, when the inverse of the susceptibility is taken (Fig. 14b), it is found that the data does not have the expected linear change with temperature ($X = \frac{C}{T-\theta}$) at higher temperatures. To determine the paramagnetic variables from the data, the following equation was applied to Fig. 14a at temperatures above 150 K:

$$X = X_0 + \frac{C}{T-\theta}$$

where C is the Curie constant, θ is the Weiss Constant and χ_o is the temperature independent susceptibility. The fitting gave C = 0.499 emu.K/mol.Oe, θ = −18.3 K and χ_o = 0.00704 emu/mol.Oe. At temperatures above 150 K, the ac susceptibility is dominated by the temperature independent component, as the measured value is 0.0108 emu/mol.Oe or less. Thus, the independent susceptibility component makes up over 65% of the measured value. This component could be due to the ferromagnetic phase observed in Fig. 12 inset. As the ferromagnetic component is observed at 300 K, this means that the measurement is taking place below the ferromagnetic-paramagnetic transition at the Curie temperature. In this region, it is where the ferromagnetic susceptibility has plateaued, and is weakly dependent on temperature. Thus, at the low applied field of the temperature measurement, at the higher temperatures, the ferromagnetic component dominates the susceptibility response, as a temperature independent susceptibility.

For the imaginary susceptibility part, only the 1000 Hz data shows anything within the noise, this is a change at ~20 K, which is in good agreement with the Weiss constant determined from the fitting to the real ac component. No peak is observed in the real ac susceptibility data, which would be expected for an antiferromagnetic transition. The effective moment was calculated using the equation $\mu_{eff} = 2.828\sqrt{XT}$ (Fig. 14c). Where at high temperature (>200 K), the effective moment is normally a constant for a paramagnetic compound, but for the as-measured sample the effective moment decreases as the temperature decreases. Hence, at 300 K, it is measured as 4.5 μ_B. If the effective moment was purely from the Cu^{2+}ions, then it is expected to be between 1.9 and 2.1 μ_B. The calculated value using the given equation is more than the double, which suggests that the ferromagnetic component also contributes as well. Another method of determining the effective moment is to apply the equation $\mu_{eff} = 2.828\sqrt{C}$. If the value of C is taken from the above derived parameters fitted to the real component susceptibility, then the effective moment is 2 μ_B, which is in the expected range. This means that the susceptibility at the higher temperatures is dominated by an independent component, which masks the Cu^{2+}ions contribution to the susceptibility. Further, when the temperature independent susceptibility is subtracted away from the real susceptibility, and the inverse is plotted as a function of temperature (Fig. 14b), then it is observed that there is now a linear dependence with temperature at temperatures > 150 K, although the data is noisy. Fitting Curie's law to the high temperature data in Fig. 14b, now gives C = 0.495 and θ = −18 K, so close to those measured on the data in Fig. 14a. Fig. 14c gives the effective moment of the sample after the independent susceptibility has been substrate, and it is observed that the average effective moment at high temperature is ~ 2.07μ_B, which is in the expected range for Cu^{2+}ions.

3.7. Molecular geometry

The optimized geometric parameters of complex $[Cu_2(ox)(dien)_2](NO_3)_3$ are listed in Table 6. The calculated bond lengths in the vicinity of the metallic center are found to be varying from 2.1026 to 2.2746 Å, whereas the experimental ones are in the range [1.993(2)−2.007(2)] Å. These values agree well, with a with maximum deviation values of 0.2676 Å and 0.2707 Å observed respectively for the Cu1—N1 and Cu2—N14 bonds. Furthermore, the mean <Cu—N> and <Cu—O> values are computed to be respectively <2.1472> Å and <2.1138> Å. Correspondingly, the related experimental ones are respectively being equal to <2.0009> Å and <2.4033> Å. On the other hand, from Table 6 the computed values of the bond angles surrounding the Cu(II) cations fall in the range 69.4–136.3°, and the corresponding experimental ones are found to be in the interval [79.54(6), 176.72(7)]°. Moreover, the mean <N—Cu—N>, <O—Cu—O> and <N—Cu—O> values of the related experimental bond angles are respectively 110.66°, 79.58° and 111.06°, which are comparable to the computed ones being

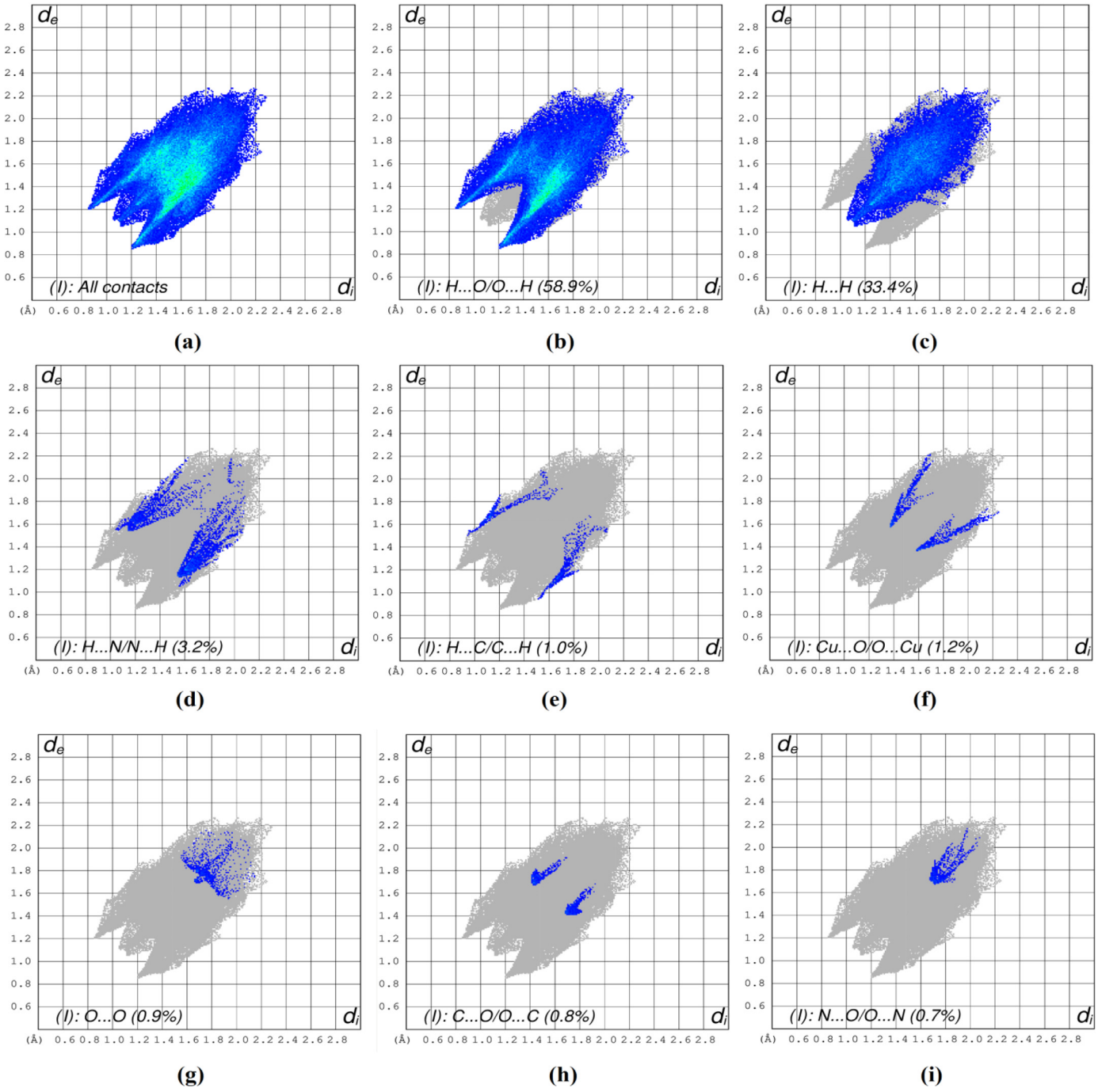

Fig. 17. Total contacts in the molecular packing of complex $[Cu_2(ox)(dien)_2](NO_3)_3$ and their decomposed 2D FPs.

equal to 102.07°, 79.58° and 104.27°, respectively. Accordingly, the maximum deviations between the experimental and computed bond angles are 31.33°, which is associated to the angle O2A—Cu1—N4 and 33.92° obtained for the bond angle N11—Cu2—O3A. Therefore, these values show a very good agreement between the optimized molecular structure and the experimental geometric parameters obtained from the single-crystal X-ray diffraction data.

3.8. FMOs and MEP maps

The contour plots of the computed frontier molecular orbitals HOMO and LUMO are depicted in Fig. 15, in which the red-colored regions represent electro-negatively rich regions, whereas the green-colored zones are electro-negatively poor. On the LUMO drawing, there are two symmetrical balloons laterally situated, wheras the HOMO representation shows increased size lobes especially around the metallic centers, which indicates their activity.

Additionally, the active regions are further defined by establishing the molecular electrostatic potential MEP map given in Fig. 16, which displays red regions surrounding the oxygen atoms of the oxalate-bridge known as nucleophilic areas, as well as blue-green gradient in the environment of the ligands' atoms.

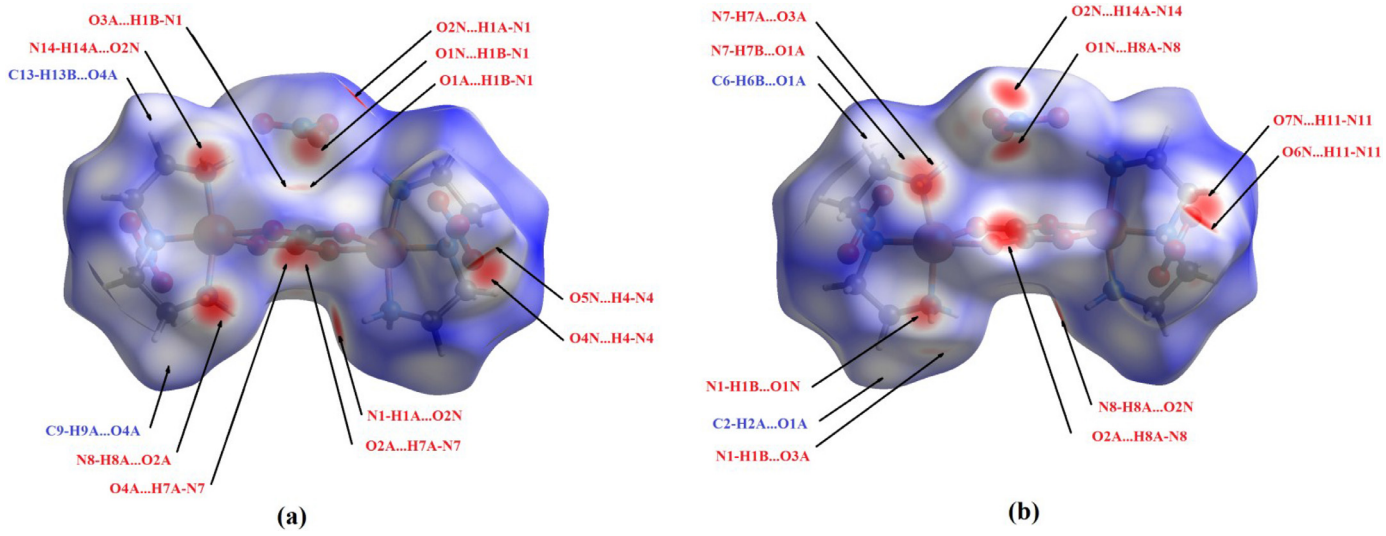

Fig. 18. (a), (b) d_{norm} representations of the HS of complex $[Cu_2(ox)(dien)_2](NO_3)_3$ showing the N–H…O and C–H…O hydrogen bonds.

3.9. Hirshfeld *surface analysis*

The overall distribution of the intermolecular interactions in the molecular packing of the title complex, as well as the decomposed FPs into the contribution of the related individual contacts are depicted in Fig. 17. It can be seen that the main leading contacts are H…O/O…H and H…H contacts with the respective contributions to the overall HS of 58.9% (Fig. 17b) and 33.4% (Fig. 17c). Additionally, H…N/N…H and H…C/C…H contacts were found to contribute to the total FP with the respective percentage of 3.2% (Fig. 17d) and 1.0% (Fig. 17e). Interestingly, the analysis of the decomposed FPs of $[Cu_2(ox)(dien)_2](NO_3)_3$ revealed that the contribution of the Cu…O/O…Cu intermolecular contacts to the total *Hirshfeld* areas is 1.2% (Fig. 17f). Whereas the other non-classical contacts, namely O…O (Fig. 17g), C…O/O…C (Fig. 17h) and N…O/O…N (Fig. 17i), show a negligible proportion of less than 1% (0.9%, 0.8% and 0.7% respectively).

In order to highlight the mentioned contacts and find out their emanating interactions, we have mapped the HS of $[Cu_2(ox)(dien)_2](NO_3)_3$ on the d_{norm} and d_i representations (Figs. 18 and 19). Consequently, the decomposed FP highlighting the H…O/O…H contacts exhibit a closest contact at about $d_i + d_e \sim$ 2.05 Å, which originated from the N8–H8A…O2A hydrogen bond (Fig. 18a). Furthermore, the same figure highlights the presence of the following strong H-bonds: N8–H8A…O2N ($d_i + d_e \sim$ 2.20 Å), N8–H8A…O1N ($d_i + d_e \sim$ 2.15 Å), N14–H14A…O2N ($d_i + d_e \sim$ 2.20 Å), N1–H1A…O2N ($d_i + d_e \sim$ 2.08 Å), N1–H1B…O1N ($d_i + d_e \sim$ 2.32 Å) and N11–H11…O6N ($d_i + d_e \sim$ 2.13 Å). In addition to the N–H…O H-bonds, the H…O/O…H contacts originate as well from the C–H…O hydrogen-bonding interactions represented among others in the shortest C2–H2A…O1A hydrogen bond being approximately 2.25 Å long (Fig. 18b). The most prominent N–H…O and C–H…O hydrogen-bonding interactions are depicted in Fig. 18.

As for the H…H contacts appearing as scattered points in the FP and spreading up from $d_i = d_e \sim$ 1.1 Å to $d_i = d_e \sim$ 2.2 Å (Fig. 17c), they showed a shortest contact with a $d_i + d_e$ value of about 2.15 Å, which could be attributed to the C10–H10B…H13A–C13 interaction (Figs. 19.a and 19b). It is worth to be noted that other short C–H…H–C interactions contribute to the H…H contacts, namely C12–H12A…H9B–C9 ($d_i + d_e \sim$ 2.20 Å) and C2–H2A…H5A–C5 ($d_i + d_e \sim$ 2.38 Å) represented in Fig. 19a, as well as short N–H…H–C and N–H…H–N interactions for instance: N1–H1A…H6A–C6, N14–H14B…H9B–C9, N4–H4…H3B–C3, N14–H14B…H1A–N1 and N14–H14B…H1B–N1 which are shown in Figs. 19a and 19b.

On the other hand, the *shape index* representation of $[Cu_2(ox)(dien)_2](NO_3)_3$ shown in Fig. 20 displayed large orange areas resulting mainly from the presence of H…N/N…H and H…C/C…H contacts. Accordingly, the H…N/N…H contacts represented as chicken wing-shaped structure in Fig. 19d showed a minimum $d_i + d_e$ value of approximately 2.60 Å, which is due to the N8–H8A…N1N and C6–H6B…N4 interactions (Fig. 20a). Whereas the H…C/C…H contacts, denoted as lateral sharp spikes in Fig. 19e, presented a shortest $d_i + d_e$ distance being around 2.47 Å long which reflects mainly the existence of the N7–H7B…C2A hydrogen bond (Fig. 20b) in addition to the N1–H1B…C1A ($d_i + d_e \sim$ 2.67 Å) and N7–H7A…C2A ($d_i + d_e \sim$ 2.65 Å) interactions (Fig. 20a). Similarly, the Cu…O/O…Cu contacts, appearing as lateral chicken wing-shaped pattern on the FP shown in Fig. 17f, exhibited a shortest Cu…*lp* interaction (Cu1…O2N) of $d_i + d_e \sim$ 2.96 Å (Figs. 20a and 20b). Moreover, the title complex was found to show closest O…O, N…O/O…N and C…O/O…C contacts at respectively 3.36 Å, 3.38 Å and 3.06 Å (Figs. 17g, 17i and 17h). These values are attributed to the *lp*…*lp* and C…*lp*/*lp*…C interactions resulting respectively from O1N…O3A/O3A…O1N, O3A…N1N/N1N…O3A and C2A…O2N/O2N…C2A and drawn in (Fig. 20).

3.10. Topological analysis

For a better description of the molecular packing of complex $[Cu_2(ox)(dien)_2](NO_3)_3$, its structural packaging will be simplified into central nodes and bridging rods by performing a topological analysis [72–76]. By considering the different atomic entities centroids composing the structure as net central nodes, we have found that the structural network of $[Cu_2(ox)(dien)_2](NO_3)_3$ could be simplified into a new unknown 5-nodal 1^4,2,3,4^4,5-connected M48–1 topology, resulting from the standard representation of covalent and ionic compounds, with the point symbol $(0)_{13}(5^2.8)_2(5^3.8)(5)_8$. This topology could be simplified further and could be sketched as a binodal 1,3-connected 1,3M4–1 underlying net having the stoichiometry (1-c)$_3$(3-c). Furthermore, if we analyze the crystal packaging of $[Cu_2(ox)(dien)_2](NO_3)_3$ over the coordination compounds and valence-bonded MOFs simplification approach, in which we consider separately the metallic centers, the oxalate bridges and the organic ligands as the net nodes, we obtain

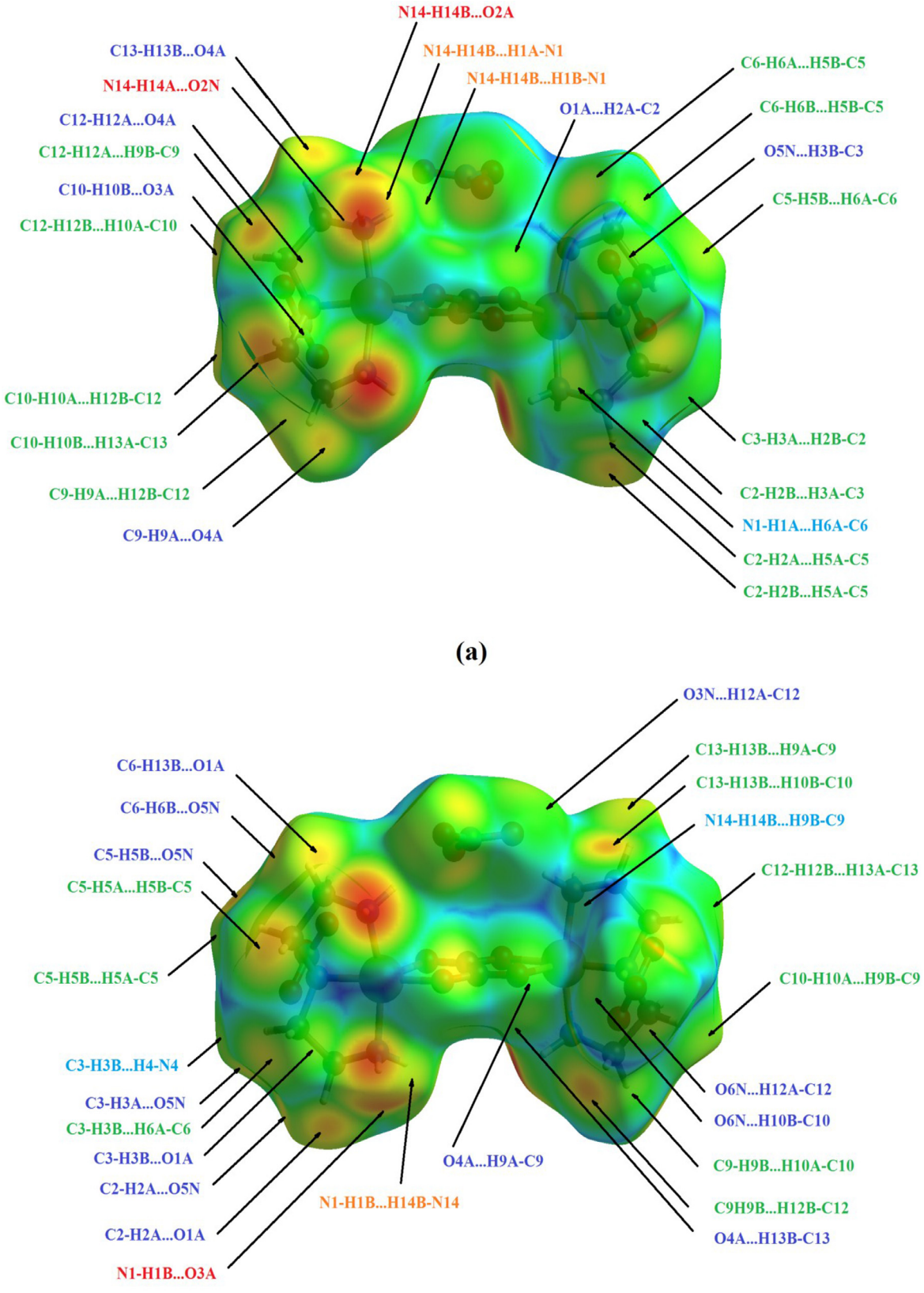

Fig. 19. (a), (b) HSs of complex $[Cu_2(ox)(dien)_2](NO_3)_3$ mapped over d_i highlighting the N–H…O, C–H…O, N–H…H–N, C–H…H–C and N–H…H–C interactions.

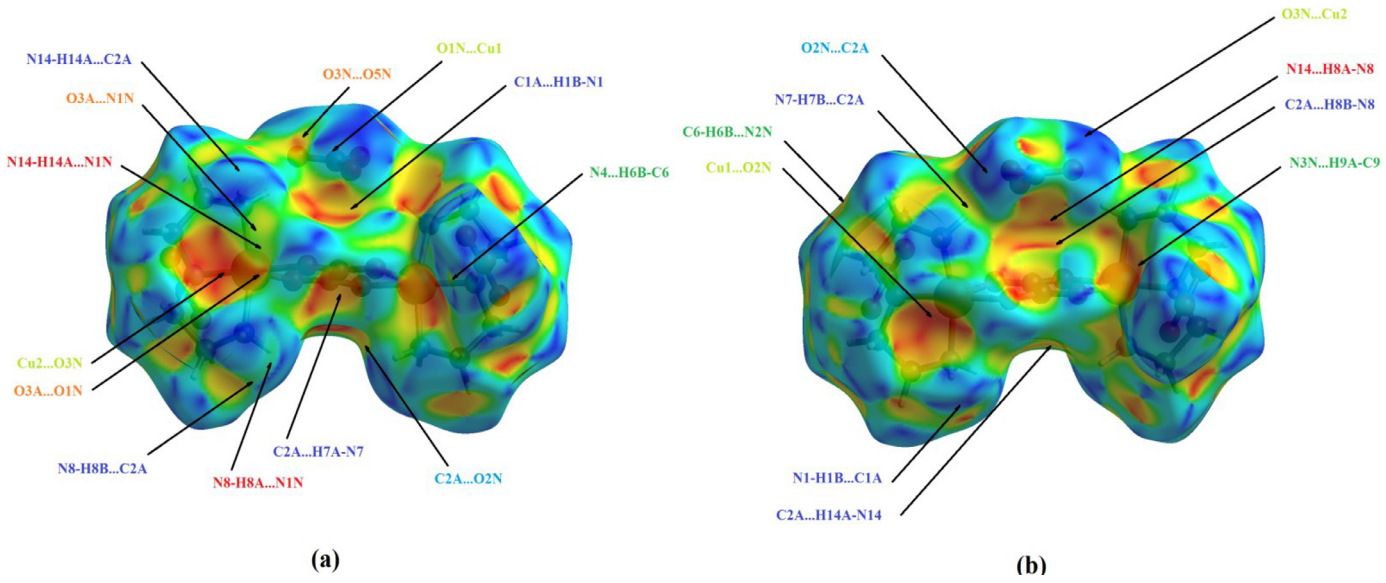

Fig. 20. (a), (b) HSs of the title complex mapped over the *shape index* function emphasizing the N–H...N, C–H...N, N–H...C, π...*lp*, *lp*...*lp* and Cu...*lp* interactions.

a standard representation defined as a trinodal 1,2,2-coordinated 1,2,2M5–1 underlying net with the $(1\text{-c})_2(2\text{-c})(2\text{-c})_2$ stoichiometry. On the other hand, the structure could be simplified by taking into consideration the different intermolecular hydrogen-bonding interactions linking the molecules together. Consequently, the standard representation of hydrogen-bonded molecular structures, supposing the nitrate counter-ions and the oxalate-bridges as H-bonds' acceptors, led to a binodal 4,8-coordinated sqc21 net, showing the point symbol $(3^2.4^2.5^2)$ $(3^4.4^8.5^{12}.6^4)$ and the stoichiometry (4-c)(8-c). As by taking into account the van der Waals networks, the simplification of $[Cu_2(ox)(dien)_2](NO_3)_3$ via the standard representation of the Coulomb or *vdW*-bonded molecular structures reduced it into a new 3-nodal 4,6,24-connected topology. The simplification methods as well as the resulting underlying nets are illustrated in Fig. 21.

3.11. Antioxidant activity of $[Cu_2(ox)(dien)_2](NO_3)_3$

The antioxidant activity of the $[Cu_2(ox)(dien)_2](NO_3)_3$ complex was evaluated using different methods: DPPH, ferric reducing power tests and the phosphomolybdenum assay. These methods differ from the mechanism of reaction involved, and the two main categories are thus: hydrogen atom abstraction (HAT) or electron transfer (ET). The DPPH radical scavenging test is a simple and rapid method to assess the antioxidant activity of a sample [77]. The scavenging activity of the $[Cu_2(ox)(dien)_2](NO_3)_3$ complex vary depending on the used concentration, hence the scavenging activity of the DPPH free radical increases with the increase of concentration (Fig. 22). In comparison with the antioxidant activity of the reference, the copper complex exerts a moderate scavenging activity. The concentration that inhibits 50% of the free radical of DPPH (IC_{50}%) is an indicator of strong antioxidant activity. However, even at a concentration of 4000 µg/mL of the complex, the IC_{50}% was not achieved in comparison with the BHT (IC_{50}= 48.32 µg/mL). Therefore, it should be noted that the antioxidant activity depends strongly on the number and position of the polyhydroxyl groups and the type of substituent [78]. Following this approach, the low scavenging activity of DPPH radical by the present copper complex could be argued by the low number of free hydroxyl units in its structure.

The FRAP (Ferric Reducing Antioxidant Power) assay measures the capacity to reduce Fe(III) to Fe(II) by donating an electron, the reaction is reproducible and linearly related to the concentration of the antioxidant tested [79]. As shown in Fig. 23, the reducing power of the $[Cu_2(ox)(dien)_2](NO_3)_3$ complex remains stable even by increasing its concentration. In comparison with the reducing activity of the gallic acid, the copper complex exhibits a very low reducing activity. The phosphomolybdenum assay is routinely applied to express the total antioxidant capacity (TAC) of a sample. Moreover, the TAC assay gives a direct estimation of reducing capacity of antioxidants based on the reduction of Mo(VI) to Mo(V) [52].

Fig. 24 shows the total antioxidant capacity of the $[Cu_2(ox)(dien)_2](NO_3)_3$ complex in comparison with that of gallic acid used as an antioxidant of reference. In the majority of cases, FRAP test and PM assay reveal a similar response whether there is low or high reducing activity. Thus, according to FRAP assay, the total antioxidant capacity of the $[Cu_2(ox)(dien)_2](NO_3)_3$ complex using phosphomolybdenum assay revealed as expected a low capacity compared with gallic acid. As far as we know, this is the first study that investigates the $[Cu_2(ox)(dien)_2](NO_3)_3$ complex for its antioxidant activity. The three validated methods applied in the present work complement one another and allow to give an overview of the antioxidant properties of the tested compound. As a result, the $[Cu_2(ox)(dien)_2](NO_3)_3$ complex was estimated as weak antioxidant.

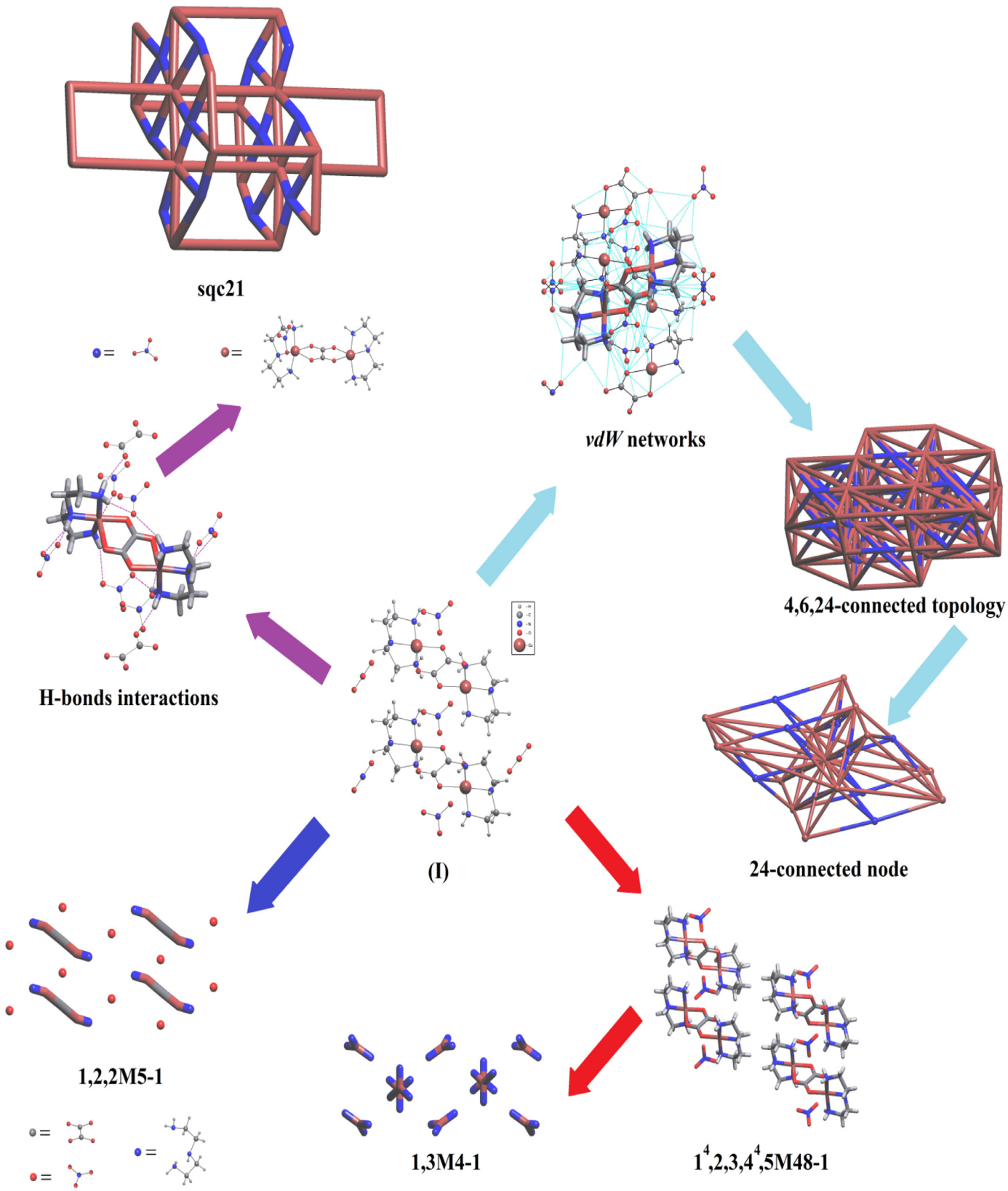

Fig. 21. Underlying nets resulting from the simplification of the molecular packing of complex $[Cu_2(ox)(dien)_2](NO_3)_3$.

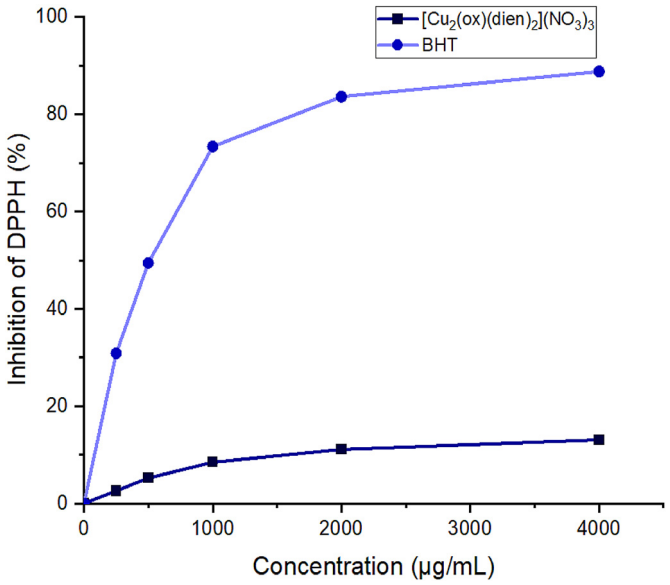

Fig. 22. DPPH radical scavenging activity of $[Cu_2(ox)(dien)_2](NO_3)_3$ complex vs. BHT.

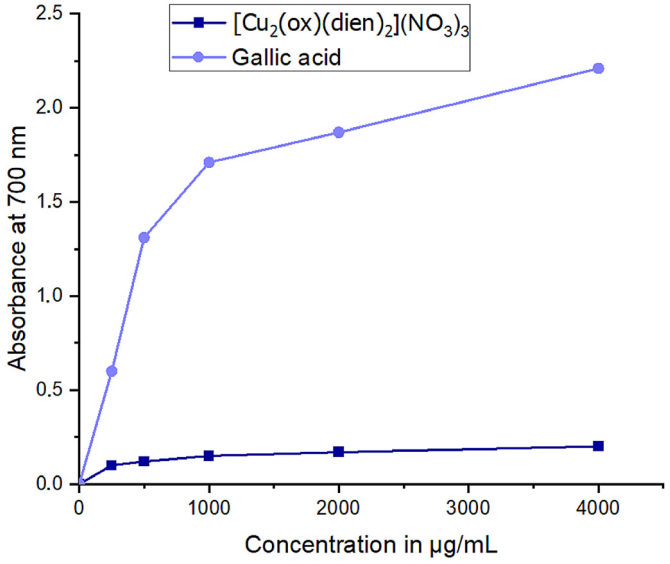

Fig. 23. Reducing power of $[Cu_2(ox)(dien)_2](NO_3)_3$ complex vs. gallic acid.

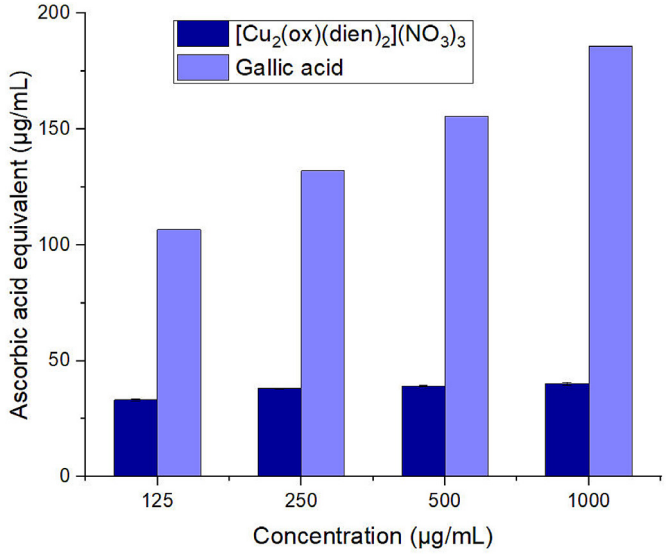

Fig. 24. Total antioxidant capacity of the $[Cu_2(ox)(dien)_2](NO_3)_3$ complex vs. gallic acid.

4. Conclusions

A new complex was synthesized under wet chemistry conditions and crystallographically characterized by means of single-crystal X-ray diffraction. The copper atoms show a distorted square–pyramidal coordination environment formed by three nitrogen atoms of the diethylenetriamine group, acting as a facially coordinated tridentate ligand, and two oxygen atoms of the bridging oxalate bidentate ligand. Thus, the geometry of the two copper atoms is penta-coordinated in a distorted coordination polyhedron close to square pyramidal, with calculated values of τ being 0.218 for Cu1 and 0.240 for Cu2. The phase purity of the studied compound was confirmed by powder XRD measurement. The experimental and calculated IR spectra of $[Cu_2(ox)(dien)_2](NO_3)_3$ were compared and therefore the absorption bands were associated to the related vibration modes in the complex. In addition, the electronic spectrum of the complex showed an intense band, at 332 nm in solid state and at 249 nm in water solution, which result from the n–π^* transition belonging to the oxalate (C = O) group. The thermal behavior of the complex was investigated and its calcination under air led to the production of CuO nanoparticles. Moreover, the morphology and the size of the copper complex and the resulting CuO nanoparticles were monitored by scanning electron microscopy (SEM). The magnetization and ac susceptibility of the sample as a function of magnetic field and temperature were measured and fully discussed. The molecular structure of the complex was optimized at the *M06-2X/LANL2DZ* level in water. It was found that this method reproduces well the geometry of the studied complex and thus the computed geometric parameters compare well with the related experimental values. Furthermore, the examination of the frontier molecular orbitals allowed identifying the electro-negatively rich and poor regions. The HOMO orbitals located around the metallic centers indicated their activity. The intermolecular interactions in the molecular packing of the complex as well as their contributions were investigated by performing HS and topological analyses. The HSA showed that the leading contacts are H…O/O…H followed by the H···H contacts, which originate mainly from N–H…O and C–H…O hydrogen bonds as well as short C–H…H–C, N–H…H–C and N–H…H–N interactions. As for the topological analysis, it allowed simplifying the structural packaging of the studied complex which could be described as a binodal 1,3-connected 1,3M4-1 underlying net, a trinodal 1,2,2-coordinated 1,2,2M5-1 simplified net and a binodal 4,8-coordinated sqc21 net by following different simplification approaches. In addition, the antioxidant activity of the complex was evaluated using different methods, namely DPPH, ferric reducing power tests and phosphomolybdenum assay. The results showed that the complex could be considered as a weak antioxidant.

Authors contributions statement

M. Akouibaa carried out the whole research investigations in the framework of this thesis supervised by Prof. M. Lachkar, he wrote the preliminary draft. H. Oudghiri Hassani performed the catalytic part. M. Poupon and M. Dusek solved the crystal structure. B. El Bali contributed to the structural investigations, adjusted, in collaboration with M. Dusek, the structural part, and they both finalized the manuscript to the submitted version.

Declaration of Competing Interest

The authors declare no conflict of interest.

Data availability

No data was used for the research described in the article.

Acknowledgments

BEB would like to thank Dr C. Wilson (University of Glasgow, School of Chemistry, Joseph Black Building, Glasgow, UK) for the crystal structure determination. AD would like to acknowledge the fund of the Ministry of Higher Education and Scientific Research MESRS and Abbes Laghrour University of Khenchela (Algeria) under the project number: B00L01UN400120210002 (PRFU).

References

[1] J.B. Wang, M.S. Chou, Kinetics of catalytic oxidation of benzene, n-hexane, and emission gas from a refinery oil/water separator over a chromium oxide catalyst, J. Air. Waste. Manag. Assoc. 50 (2000) 227–233, doi:10.1080/10473289.2000.10464003.

[2] B.L. Treu, W.G. Fahrenholtz, M.J. O'keefe, Thermal decomposition behavior of praseodymium oxides, hydroxides, and carbonates, Inorg. Mater. 47 (2011) 974–978, doi:10.1134/S0020168511090214.

[3] I.A. Shagufta, Transition metal complexes as proteasome inhibitors for cancer treatment, Inorg. Chim. Acta. 506 (2020) 119521, doi:10.1016/j.ica.2020.119521.

[4] J. Carranza, C. Brennan, J. Sletten, B. Vangdal, P. Rillema, F. Lloreta, M. Julve, Syntheses, crystal structures and magnetic properties of new oxalato, croconato-and squarato containing copper (II) complexes, N. J. Chem. 27 (2003) 1775–1783, doi:10.1039/B301212N.

[5] J. Glerup, P.A. Goodson, D.J. Hodgson, M. Kirsten, Magnetic exchange through oxalate bridges: synthesis and characterization of (μ-Oxalato) dimetal (II) complexes of manganese, iron, cobalt, nickel, copper, and zinc, Inorg. Chem. 34 (1995) 6255–6264, doi:10.1021/ic00129a009.

[6] L.A. Dubraja, M. Jurić, F. Torić, P. Damir, The influence of metal centres on the exchange interaction in heterometallic complexes with oxalate-bridged cations, Dalton Trans. 46 (2017) 11748–11756, doi:10.1039/C7DT02522J.

[7] D. Miao, G. Ya-Mei, B. Xian-He, A novel oxalato-bridged dinuclear copper (II) complex with diazamesocyclic terminal ligand: crystal structure, spectroscopy and magnetism, Inorg. Chim. Acta. 335 (2002) 136–140, doi:10.1016/S0020-1693(02)00810-1.

[8] C.L.F. Dazem, B.N. Ndosiri, E.N. Nfor, R. Köferstein, P. Shankhari, B.P.T. Fokwa, J. Nenwa, Synthesis, structures, thermal and magnetic properties of two bis(oxalato) cuprate (II) hybrid salts containing pyridinium derivative cations, J. Mol. Struct 1203 (2020) 127399, doi:10.1016/j.molstruc.2019.127399.

[9] M.L. Calatayud, I. Castro, J. Sletten, F. Lloret, M. Julve, Syntheses, crystal structures and magnetic properties of chromato-, sulfato-, and oxalato-bridged dinuclear copper (II) complexes, Inorg. Chim. Acta. 300 (2000) 846–854, doi:10.1016/S0020-1693(99)00590-3.

[10] N.S. Ovanesyan, V.D. Makhaev, S.M. Aldoshin, P. Gredin, K. Boubekeur, C. Trainc, M. Gruselle, Structure, magnetism and optical properties of achiral and chiral two-dimensional oxalate-bridged anionic networks with symmetric and asymmetric ammonium cations, Dalton Trans. (2005) 3101–3107, doi:10.1039/B506671A.

[11] B. Zina, D. Amani, S. Koray, B. El Bali, M. Lachkar, N. BenaliCherif, Crystal structure, Hirshfeld surface analysis and theoretical calculations of an oxalato-bridged copper (II) complex: μ-oxalato-bis [(2,2'-bipyridine) hydrate copper (II) nitrate], J. Iran. Chem. Soc. 17 (2020) 671–685, doi:10.1007/s13738-019-01805-0.

[12] K.P. Strotmeyer, I.O. Fritsky, R. Ott, P. Hans, K. Roland, Evaluating the conformational role of an allosteric CuII ion in anion recognition and catalysis by a tricopper complex, Supramol. Chem. 15 (2003) 529–547, doi:10.1080/1061027031000160512 4.

[13] F.A. Mautner, F.R. Louka, S.S. Massoud, Structural characterization of some oxalato-bridged copper(II) and nickel(II) complexes, J. Mol. Struct. 921 (2009) 333–340, doi:10.1016/j.molstruc.2009.01.031.

[14] J.-X. Li, Z.-X. Du, L.-L. Zhang, D.-L. Liu, Q.-Y. Pan, doubly mononuclear cocrystal and oxalato-bridged binuclear copper compounds containing flexible 2-((3,5,6-trichloropyridin-2-yl) oxy) acetate tectons: synthesis, crystal analysis and magnetic properties, Inorg. Chim. Acta 512 (2020) 119890, doi:10.1016/j.ica.2020.119890.

[15] O. Castillo, A. Luque, F. Lloret, R. Pascual, One-dimensional oxalato-bridged copper (II) complex possessing two structurally different metallic centres, Inorg. Chem. Commun. 4 (2001) 350–353, doi:10.1016/S1387-7003(01)00209-X.

[16] S.V. Tomyn, E. Gumienna-Kontecka, I.O. Fritsky, T.S. Iskenderov, J. Świątek-Kozłowska, μ-Oxalato-1κ2O,O′:2κ2O″,O‴-bis(chloro{[1-(2-*pyridyl*-κN)*ethylidene*]hydrazine κN}copper(II)), Acta Crystallogr. Sect. E: Struct. Rep. 63 (2007) m438–m440, doi:10.1107/S1600536807000098.

[17] J.L. Shaw, G.T. Yee, G. Wang, D.E. Bensom, C. Gokdemir, C.J. Ziegler, Magneto-structural relationships in a series of dinuclear oxalato-bridged (diphenyldipyrazolylmethane) copper (II) complexes, Inorg. Chem. 44 (2005) 5060–5067, doi:10.1021/ic048229t.

[18] F.R. Louka, F.A. Mautner, R. Vicente, S.S. Massoud, μ2-Oxalato-bridged tricopper (II) complex derived from 1,4,8,12-tetraazacyclopentadecane: synthesis, structure and magnetic characterization, Inorg. Chem. Commun. 11 (2008) 438–441, doi:10.1016/j.inoche.2008.01.019.

[19] J. Carranza, H. Grove, J. Sletten, F. Lloret, M. Julve, P. Kruger, E. Chad, R. Paul, Synthesis, X-ray crystal structure and magnetic properties of oxalato-bridged copper (II) complexes with 2,3-bis(2-pyridyl) pyrazine,2,3-bis (2-pyridyl) quinoxaline and 2,2′bipyrazine as peripheral ligands, Eur. J. Inorg. Chem. (2004) 4836–4848 2004, doi:10.1002/ejic.200400500.

[20] Y. Sujittra, C. Achareeya, D. Chanaiporn, C. Narongsak, P. Chaveng, A.V.A. Gerard, R. Jan, Two new oxalato-bridged dinuclear copper(II) complexes with di-2-pyridylamine: crystal structures, spectroscopic and magnetic properties, Inorg. Chem. Commun. 9 (2006) 973–977, doi:10.1016/j.inoche.200.05.022.

[21] F. Castiñeiras, R. Dominguez, L. Gómez-Rodriguez, J. Borrás, Z. Anorg, Magnetic exchange interactions in dinuclear copper (II) and nickel (II) complexes with μ-oxalato bridges. The structure of μ-Oxalato(O,O′,O″,O‴)-bis{[1,8-di(2-pyridyl)-3,6- dithiaoctane-N,N′,S,S′] nickel (II)} dinitrate dihydrate, Z. Anorg. Allg. Chem. ZAAC. 629 (2003) 1096–1103, doi:10.1002/zaac.200300058.

[22] S. Youngme, P. Gunnasoot, C. Narongsak, C. Pakawatchai, Dinuclear copper (II) complexes with ferromagnetic and antiferromagnetic interactions mediated by a bridging oxalato group: structures and magnetic properties of [Cu2L4(μ-C2O4)](PF6)2(H2O)2 and [Cu2L2(μ-C2O4)(NO3)2((CH3)2NCOH)2](L= di-2-pyridylamine), Transit. Met. Chem. 29 (2004) 840–846, doi:10.1007/s11243-004-1566-9.

[23] J.K. Tang, E.Q. Gao, L. Zhang, L. Dai-Zheng, J. Zong-Hui, Y. Shi-Ping, Synthesis, crystal structure and magnetic properties of an oxalato-bridged dinickel (II) complex containing a macrocyclic ligand, J. Coord. Chem. 55 (2002) 527–535, doi:10.1080/0095870290020838.

[24] M. Du, Y.M. Guo, S.T. Chen, X.H. Bu, J. Ribas, Crystal structures, spectra and magnetic properties of di-2-pyridylamine (dpa) CuII complexes [Cu(dpa)2(N3)2](H2O)2 and [Cu2(μ-ox)(dpa)2(CH3CN)2](ClO4)2, Inorg. Chim. Acta. 346 (2003) 207–214, doi:10.1016/S0020-1693(02)01430-5.

[25] R. Wen, I. Bernal, S.S. Massoud, R.K. Thalji, D.R. Billodeaux, F.R. Fronczek, Crystal structures and magnetic studies of six new nickel (II) amine μ-oxalato compounds, Inorg. Chim. Acta. 295 (1999) 91–105, doi:10.1016/S0020-1693(99)00328-X.

[26] R. Cao, S. Liu, L. Xie, Y. Pan, J. Cao, Y. Ren, L. Xu, Organic-inorganic hybrids constructed of anderson-type polyoxoanions and oxalato-bridged dinuclear copper complexes, Inorg. Chem 46 (2007) 3541–3547, doi:10.1021/ic062208c.

[27] K. Mochzuki, Y. Numata, Y. Kitazawa, A. Ishil, Structure and properties of an oxalato-bridged dinickel (II) complex with a tetraazamacrocycle bearing an aminomethyl pendant arm, 5-aminomethyl-5R(S), 12R(S)-dimethyl-1,4,8,11-tetraazacyclotetradecane, J. Coord. Chem. 57 (2004) 543–551, doi:10.1080/00958970410001677042.

[28] P. Román, C. Guzmán-Miralles, A. Luque, J.I. Beitia, J. Cano, F. Lloret, M. Julve, S. Alvarez, Influence of the peripheral ligand atoms on the exchange interaction in oxalato-bridged nickel (II) complexes: an orbital model. Crystal structures and magnetic properties of (H3dien)2[Ni2(*ox*)5].12H2O and [Ni2(dien)2(H2O)2(ox)] Cl2, Inorg. Chem. 35 (1996) 3741–3751, doi:10.1021/ic951081g.

[29] A. Escuer, R. Vicente, M.S. El Fallah, J. Joel, Magnetic studies on the μ-oxalato nickel (II) dimers with an [NiN4O2] environment. Crystal structure of (μ-ox)-[Ni(323-*tet*)]2(ClO4)2·2H2O (323-tet= N,N′-bis (3-aminopropyl)-1,2-ethanediamine), Inorg. Chim. Acta. 232 (1995) 51–156, doi:10.1016/0020-1693(94)04378-9.

[30] J.L. Shaw, G.T. Yee, G. Wang, E.B. David, G. Cagil, J.Z. Christopher, Magneto-Structural Relationships in a Series of Dinuclear Oxalato-Bridged (Diphenyldipyrazolylmethane) copper (II) Complexes, Inorg. Chem. 44 (2005) 5060–5067, doi:10.1021/ic048229t.

[31] R.N. Patel, N. Singh, K.K. Shukla, U.K. Chauhan, S. Chakraborty, J. Niclós-Gutiérrez, A. Castiñeiras, X-ray, spectral and biological (antimicrobial and superoxide dismutase) studies of oxalato bridged CuII–NiII and CuII–ZnII complexes with pentamethyl-diethylenetriamine as capping ligand, J. Inorg. Biochem. 98 (2004) 231–237, doi:10.1016/j.jinorgbio.2003.10.003.

[32] I. Castro, M.L. Calatayud, J. Sletten, F. Lloret, M. Julve, Crystal structures and magnetic properties of the squarate-O1, On-bridged dinuclear copper (II) complexes [Cu2(phen)4 (C4O4)](CF3SO3)2·3H2O (n= 2) and [Cu2(bipy)4 (C4O4)](CF3SO3)2·6H2O (n=3), Inorganica Chim. Acta. 287 (1999) 173–180, doi:10.1016/S0020-1693(99)00011-0.

[33] I. Castro, M.L. Calatayud, J. Sletten, F. Lloret, M. Julve, Syntheses, crystal structures and magnetic properties of [Ni2(C2O4)(tren)2][ClO4]2 and [Ni2(C4O4)(tren)2 (H2O)2][ClO4]2 [tren= tris (2-aminoethyl) amine], J. Chem. Soc., Dalton Trans. (1997) 811–818, doi:10.1039/A606105B.

[34] B. Bag, N. Mondala, S. Mitra, V. Gramlich, J. Ribas, M.S. El Fallahc, Synthesis, crystal structure and magnetic properties of a new oxalato-bridged binuclear copper (II) complex with a tridentate Schiff base ligand, Polyhedron 20 (2001) 2113–2116, doi:10.1016/S0277-5387(01)00707-0.

[35] L.I. Yan-Tuan, Y. Cui-Wei, G. Hua-Shi, Synthesis and magnetic studies of oxalato-bridged copper(II) chromium(III) copper(II) and copper(II) iron(III) copper(II) heterotrinuclear complexes, Polyhedron 22 (2003) 3223–3230.

[36] L. Jun-Xia, D. Zhong-Xiang, Z. Lu-Lu, D. Li-Liu, Q.Y. Panac, Doubly mononuclear cocrystal and oxalato-bridged binuclear copper compounds containing flexible 2-((3,5,6-trichloropyridin-2-yl)oxy) acetate tectons: synthesis, crystal analysis and magnetic properties, Inorg. Chim. Acta. 512 (2020) 119890, doi:10.1016/j.ica.2020.119890.

[37] S. Somaye, R. Zohreh, S. Fereshteh, A paramagnetic oxalato-bridged binuclear copper(II) complex as an effective catalase inhibitor. Spectroscopic and molecular docking studies, J. Mol. Struct. 1208 (2020) 127865, doi:10.1016/j.molstruc.2020.127865.

[38] S. Youngme, G.A. van Albada, N. Chaichit, P. Gunnasoot, P. Kongsaeree, I. Mutikainen, O. Roubeau, J. Reedijk, U. Turpeinen, Synthesis, spectroscopic characterization, X-ray crystal structure and magnetic properties of oxalato-bridged

copper (II) dinuclear complexes with di-2-pyridylamine, Inorg. Chim. Acta 353 (2003) 119–128, doi:10.1016/S0020-1693(03)00207-X.
[39] M. Akouibaa, N. Hamdi, H.O. Hassani, S. Rakib, M. Lachkar, I. da Silva, B. El Bali, [Ni (N2H5)2(C2O4)2].2H2O: formation, crystal structure, catalytic performance and sorbence activities, Phys. B: Condens. Matter 635 (2022) 413857, doi:10.1016/j.physb.2022.413857.
[40] S. Chaouch, R. Ouarsal, M. Akouibaa, S. Rakib, M. Lachkar, B. El Bali, M. Dusek, Cs2[M(H2O)6]3(HPO3)4, M= Co, Ni: crystal structures, IR and thermal studies, J. Phys. Conf. Ser. 984 (2018) 12–15, doi:10.1088/1742-6596/984/1/012015.
[41] S. Hidaoui. N. Hamdi, M. Akouibaa, R. Benali-Cherif, E. Vaclav, M. Dusek, B. El Bali, Synthesis, crystal structure and catalytic activity of the new hybrid phosphate (C4H12N2)[Co(H2O)6](HPO4)2, J. Mol. Struct 1265 (2022) 133296, doi:10.1016/j.molstruc.2022.133296.
[42] M. Akouibaa, H.O. Hassani, R. Ouarsal, S. Rakib, M. Lachkar, M. Poupon, M. Dusek, N. Morley, B. El Bali, (H3dien)[Ni(NO3)(C2O4)2]. 2H2O: synthesis, crystal structure, catalytic activity and magnetic study, Chem. Data Collect. (2022) 100969, doi:10.1016/j.cdc.2022.100969.
[43] Y.C. Zhang, J.Y. Tang, G.L. Wang, M. Zhang, X.Y. Hu, Tailor the crystal shape in high-temperature solution resulted in a simultaneous growth of CuO and Cu2O, J. Cryst. Growth. 294 (2006) 278–282, doi:10.1016/j.jcrysgro.2006.06.038.
[44] I. Prakash, P. Muralidharan, N. Nallamuthu, M. Venkateswarlu, N. Satyanarayana, Nanocrystallite size cuprous oxide: characterization of copper nanopowders after natural aging, Mater. Res. Bull. 42 (2007) 1619–1624, doi:10.1016/j.materresbull.2006.11.038.
[45] G.M. Sheldrick, Crystal structure refinement with SHELXL, Acta Cryst. C71 (2015) 3–8, doi:10.1107/S2053229614024218.
[46] G.M. Sheldrick, A short history of SHELX, Acta Cryst A64 (2008) 112–122, doi:10.1107/S0108767307043930.
[47] O.V. Dolomanov, L.J. Bourhis, R.J. Gildea, J.A. Howard, H. Puschmann, OLEX2: a complete structure solution, refinement and analysis program, J. Appl. Cryst. 42 (2009) 339–341, doi:10.1107/S0021889808042726.
[48] K. Brandenburg, K.H. Putz, DIAMOND. Version 3, Crystal Impact GbR, Bonn, Germany, 2005.
[49] N. Jingyang, Z. Shaowei, C. Huanni, Z. Junwei, M. Pengtao, W. Jingping, 1-D, 2-D, and 3-D organic-inorganic hybrids assembled from Keggin-type polyoxometalates and 3d-4f heterometals, Cryst. Growth Des. 11 (2011) 3769–3777, doi:10.1021/cg2001249.
[50] R. Scherer, H.T. Godoy, Antioxidant activity index (AAI) by the 2,2-diphenyl-1-picrylhydrazyl method, Food Chem. 112 (2009) 654–658, doi:10.1016/j.foodchem.2008.06.026.
[51] M. Oyaizu, Studies on products of browning reaction, Jpn. J. Nutr. Dietet. 44 (1986) 307–315, doi:10.5264/eiyogakuzashi.44.307.
[52] P. Prieto, M. Pineda, M. Aguilar, Spectrophotometric quantitation of antioxidant capacity through the formation of a phosphomolybdenum complex: specific application to the determination of vitamin E, Anal. Biochem. 269 (1999) 337–341, doi:10.1006/abio.1999.4019.
[53] P. Chavan, L.R. Naik, P.B. Belavi, G. Chavan, C.K. Ramesha, R.K. Kotnala, Studies on electrical and magnetic properties of Mg-substituted nickel ferrites, J. Electron. Mater. 46 (2017) 188–198, doi:10.1007/s11664-016-4886-6.
[54] R.D. Dennington II, T.A. Keith, J.M. Millam, GaussView 6.0, Wallingford, 2016 CT.
[55] M.J. Frisch, G.W. Trucks, H.B. Schlegel, G.E. Scuseria, M.A. Robb, J.R. Cheeseman, G. Scalmani, V. Barone, B. Mennucci, G.A. Petersson, H. Nakatsuji, M. Caricato, X. Li, H.P. Hratchian, A.F. Izmaylov, J. Bloino, G. Zheng, J.L. Sonnenberg, M. Hada, M. Ehara, K. Toyota, R. Fukuda, J. Hasegawa, M. Ishida, T. Nakajima, Y. Honda, O. Kitao, H. Nakai, T. Vreven, J.A. Montgomery Jr., J.E. Peralta, F. Ogliaro, M. Bearpark, J.J. Heyd, E. Brothers, K.N. Kudin, V.N. Staroverov, R. Kobayashi, J. Normand, K. Raghavachari, A. Rendell, J.C. Burant, S.S. Iyengar, J. Tomasi, M. Cossi, N. Rega, J.M. Millam, M. Klene, J.E. Knox, J.B. Cross, V. Bakken, C. Adamo, J. Jaramillo, R. Gomperts, R.E. Stratmann, O. Yazyev, A.J. Austin, R. Cammi, C. Pomelli, J.W. Ochterski, R.L. Martin, K. Morokuma, V.G. Zakrzewski, G.A. Voth, P. Salvador, J.J. Dannenberg, S. Dapprich, A.D. Daniels, Ö. Farkas, J.B. Foresman, J.V. Ortiz, J. Cioslowski, D.J. Fox, Gaussian 09, Gaussian AS64L-G09RevD.01, Gaussian, Inc., Wallingford CT, 2010.
[56] M.J. Turner, J.J. MacKinnon, S.K. Wolff, D.J. Grimwood, P.R. Spackman, D. Jayatilaka, M.A. Spackma, Crystal Explorer Ver. 17.5, University of Western Australia, 2017 http://crystalexplorer.scb.uwa.edu.au.
[57] V.A. Blatov, A.P. Shevchenko, D.M. Proserpio, Applied topological analysis of crystal structures with the program package, ToposPro. Cryst. Growth Des. 14 (2014) 3576–3586, doi:10.1021/cg500498k.
[58] A.W. Addison, T. Rao, R. Nageswara, V.N.Jacobus Jan, C.V. Gerrit, Synthesis, structure, and spectroscopic properties of copper (II) compounds containing nitrogen-sulphur donor ligands; the crystal and molecular structure of aqua [1,7-bis(N-methylbenzimidazol-2′-yl)-2,6-dithiaheptane] copper (II) perchlorate, J. Chem. Soc., Dalton Trans. 7 (1984) 1349–1356, doi:10.1039/DT9840001349.
[59] R. Kumar, T. Guchhait, V. Subramaniyan, G. Mani, Mixed ligand Cu(II) complexes: square pyramidal vs trigonal bipyramidal with the pyrrole-based dipodal ligand having hydrogen bond acceptors, J. Mol. Struct. 1195 (2019) 1–9, doi:10.1039/DT9840001349.
[60] K. Robinson, G.V. Gibbs. P.H. Ribbe, Quadratic elongation: a quantitative measure of distortion in coordination polyhedra, Science 172 (1971) 567–570, doi:10.1016/j.molstruc.2019.05.087.
[61] M.E. Fleet, Z. Kristallogr. (1992) 202:51.
[62] M. Julve, M. Verdaguer, A. Gleizes, M. Philoche-Levisalles, O. Kahn, Design of. μ-oxalato copper (II) binuclear complexes exhibiting expected magnetic properties, Inorg. Chem. 23 (1984) 3808–3818, doi:10.1021/ic00191a028.
[63] D.J. Goebbert, E. Garand, T. Wende, R. Bergmann, G. Meijer, K.R. Asmis, D.M. Neumark, Infrared spectroscopy of the microhydrated nitrate ions (NO3)−(H2O)1−6, J. Phys. Chem. A. 113 (2009) 7584–7592, doi:10.1021/jp9017103.
[64] F. Öztürk, İ. Bulut, Y. Bekiroğlu, A. Bulut, Spectroscopic, structural, electrochemical and anti-microbiological studies of Cu(II)-sulfathiazole complex with diethylenetriamine ligand, Polyhedron 119 (2016) 420–428, doi:10.1016/j.poly.2016.07.019.
[65] G. Alzuet, S. Ferrer-Llusar, J. Borrás, R. Martıńez-Mánez, New Cu(II) and Zn(II) complexes of benzolamide with diethylenetriamine: synthesis, spectroscopy and X-ray structures, Polyhedron 19 (2000) 725–730, doi:10.1016/S0277-5387(00)00319-3.
[66] S. Bhattacharyya, S.B. Kumar, S.K. Dutta, E.R.T. Tiekink, M. Chaudhury, Zinc(II) and Copper(II) Complexes of Pentacoordinating (N4S) Ligands with Flexible Pyrazolyl Arms: syntheses, Structure, and Redox and Spectroscopic Properties, Inorg. Chem 35 (1996) 1967, doi:10.1021/ic950594k.
[67] Z. Mahendrasinh, S. Ankita, Sujit B. Kumar, A. Escuer, E. Suresh, Cyanato bridged binuclear nickel(II) and copper(II) complexes with pyridylpyrazole ligand: synthesis, structure and magnetic properties, Inorganica. Chim. Acta 375 (2011) 333–337, doi:10.1016/j.ica.2011.05.027.
[68] K. Sumeet, K.O. Animesh, B. Dipjyoti, D. Jayanta, K. Ashok, H. Anil, Facile synthesis of CuO nanowires and Cu2O nanospheres grown on rGO surface and exploiting its photocatalytic, antibacterial and super-capacitive properties, Phys. B: Condens. Matter. 558 (2019) 74–81, doi:10.1016/j.physb.2019.01.040.
[69] F. Bakhtiari, E. Darezereshki, One-step synthesis of tenorite (CuO) nanoparticles from Cu4 (SO4)(OH)6 by direct thermal-decomposition method, Mater. Lett. 65 (2011) 171–174, doi:10.1016/j.matlet.2010.09.071.
[70] G. Wang, J. Huang, S. Chen, Y. Gao, D. Cao, Preparation and supercapacitance of CuO nanosheet arrays grown on nickel foam, J. Power Sources. 196 (2011) 5756–5760, doi:10.1016/j.jpowsour.2011.02.049.
[71] S.-J. Wang, F. Bigdeli, X.-W. Yan, L. Esrafili, K.-G. Liu, H. Ghasempour, X.-Q. Cai, M.-L. Hu, A. Morsali, Synthesis of a new binuclear Cu(II) complex: a precise sensor for H2O2 and a proper precursor for preparation of the CuO nanoparticles, J. Organomet. Chem 926 (2020) 121507, doi:10.1016/j.jorganchem.2020.121507.
[72] L. Carlucci, G. Ciani, D.M. Proserpio, Coord. Chem. Rev. 246 (2003) 247–289, doi:10.1016/S0010-8545(03)00126-7.
[73] L. Carlucci, G. Ciani, D.M. Proserpio, CrystEngComm 5 (2003) 269–279, doi:10.1039/B305246J.
[74] I.A. Baburin, V.A. Blatov, L. Carlucci, G. Ciani, D.M. Proserpio, J. Solid State Chem. 178 (2005) 2452–2474, doi:10.1016/j.jssc.2005.05.029.
[75] V.A. Blatov, L. Carlucci, G. Ciani, D.M. Proserpio, CrystEngComm 6 (2004) 377–395, doi:10.1039/B409722J.
[76] O. Delgado-Friedrichs, D. Foster, M.M. O'Keeffe, D.M. Proserpio, M.M.J. Treacy, O.M. Yaghi, J. Solid State Chem. 178 (2005) 2533–2554, doi:10.1016/j.jssc.2005.06.037.
[77] E. González-Burgos, M. Liaudanskas, J. Viškelis, V. Žvikas, V. Janulis, M.P. Gómez-Serranillos, Antioxidant activity, neuroprotective properties and bioactive constituents analysis of varying polarity extracts from Eucalyptus globulus leaves, J. Food. Drug. Anal. 26 (2018) 1293–1302, doi:10.1016/j.jfda.2018.05.010.
[78] I. Biskup, I. Golonka, A. Gamian, Z. Sroka, Summary antioxidant activity of selected phenols estimated by ABTS and FRAP methods, Postepy Hig. Med. Doświad. 67 (2013) 958–963.
[79] R. Sharadanand Phatak, A. Subhash Hendre, C. Rohan Sharadanand Phatak, Total antioxidant capacity (TAC) of fresh leaves of Kalanchoe pinnata, J. Pharmacogn. Phytochem. 2 (2014) 32–35.